



A new tsunami hazard assessment for eastern Makran subduction zone by considering splay faults and applying stochastic modeling

Payam Momeni ^a, Katsuichiro Goda ^a, Mohammad Mokhtari^b and Mohammad Heidarzadeh^c

^aDepartment of Earth Sciences, University of Western Ontario, London, ON, Canada; ^bInternational Institute of Earthquake Engineering and Seismology (IIEES), Tehran, Iran; ^cDepartment of Architecture and Civil Engineering, University of Bath, Bath, UK

ABSTRACT

Tsunami hazard imposed by possible rupture of splay faults is important as it may significantly intensify tsunami heights locally. The Makran Subduction Zone (MSZ) in the northwestern Indian Ocean can generate large thrust earthquakes that could trigger significant tsunamis. In this paper, the effects of possible rupture of splay faults on the tsunami hazards of eastern MSZ are studied by developing a framework that uses stochastic earthquake rupture models and considers uncertainties related to rupture location, rupture geometry, seismic moment split ratio, earthquake slip asperity location within a fault plane, and earthquake slip heterogeneity. To quantify these uncertainties, 484 different parameter combinations of tsunami sources are considered systematically. The geometry of splay faults is developed using the most recent marine seismic surveys of the tectonic structure of the MSZ. A moment magnitude of 8.6 is considered as a scenario magnitude. The results of this study are generated in two parts, by considering average sources and stochastic sources. Results show significant local amplification of the maximum tsunami heights due to splay faults. For instance, the maximum wave height in Pasni, Pakistan can be amplified by a factor of four due to a single splay fault rupture scenario of average sources.

ARTICLE HISTORY

Received 4 May 2022
Accepted 19 August 2022

KEYWORDS

Earthquake; tsunami hazard; Makran subduction zone; stochastic source model; splay faults

1. Introduction

The occurrences of the 2004 Indian Ocean tsunami and the 2011 Tohoku earthquake and tsunami in the last two decades clearly demonstrated the importance of thorough assessments of tsunami hazards for subduction zones around the world. This is of particular importance for less-studied subduction zones, such as the Makran Subduction Zone (MSZ) in the northwestern Indian Ocean. Splay faults are steeply-dipping faults that branch from the main subduction plate interface during large earthquakes or can occur independently of plate-boundary events (Heidarzadeh, Pirooz, and Zaker 2009; Heidarzadeh et al. 2021; Plafker 1972). Splay faults pose significant tsunami hazards to their nearby regions because they can locally intensify tsunami heights (Hsu et al. 2006; Wang and Hu 2006).

The 1964 Alaska earthquake with a moment magnitude (M_w) of 9.2 was one of the first-recorded events that showed the potential significant tsunami hazards associated with splay faults. During that event, crustal vertical deformation of 12 m was reported from the local area that hosted the Patton Bay splay fault, whereas the maximum vertical crustal deformation of 6 m was reported in the surrounding areas that were only impacted by the rupture on the plate boundary (Fukao 1979; Plafker 1972). Similar splay faulting incidents have been suggested for the southern Cascadia

subduction zone based on paleoseismic observations (Clarke and Carver 1992). In addition, evidence was presented for the possibility of splay fault ruptures and their significant impacts during other major earthquake and tsunami events, such as the 1944 Tonankai, the 1946 Nankai, and the 2004 Sumatra-Andaman events (Cummins and Kaneda 2000; Sibuet et al. 2007). Recently, Heidarzadeh et al. (2021) reported a high potential for splay faulting in the Molucca Sea, Indonesia.

Since splay faults are relatively weak zones, they can be chosen as pathways for rupture propagation of earthquakes from the main subduction interface. Although it is possible that the interseismic elastic strains of the subduction zones could be fully released by the splay fault ruptures, it is more likely that the earthquake rupture initiates on the main subduction zone interface followed by slip partitioning between the subduction zone plate boundary and splay faults (Park et al. 2002). Kame and Yamashita (1999) showed that due to the stress field of the accretionary prism, earthquake rupture that propagates up-dip from the nucleation of great interplate earthquakes in the subduction zones tends to branch into the accretionary prism and partition between steeply-dipping thrust splay faults and the main subduction plate interface. This partitioning is more likely to occur in the parts of the accretionary prism where the horizontal

compression stress due to the subduction is the major component of the stress field. These parts include the early-stage accretionary prism near the trench line and the landward side of topographic highs which do not experience significant overburden pressure compared to their horizontal compression stress (Kame and Yamashita 1999). Although it is unknown if the splay faults can rupture occasionally by themselves, a recent study on the 2019 Mw 7.2 Molucca Sea earthquake showed that the splay faults in that region can generate tsunamis (Heidarzadeh et al. 2021; Sykes and Menke 2006). Due to their steep dip angles, splay ruptures result in significant vertical deformation of the seabed and can generate large tsunamis. The rupture of splay faults usually affects near-field local areas due to their smaller sizes compared to the plate boundary faults (Heidarzadeh, Pirooz, and Zaker 2009). In the MSZ, several splay faults have been located both in the eastern and western parts of the subduction zone (Grando and McClay 2007; Mokhtari, Fard, and Hessami 2008; Mokhtari 2015; Smith et al. 2012). Due to the presence of splay faults in the MSZ and considering significant tsunamis that splay faults have caused in other subduction zones, the effects of splay fault ruptures on tsunami hazards need to be studied for the Makran region.

Earthquake and tsunami hazard assessments for the MSZ and nearby coastal areas of Pakistan, Iran, Oman, and western India were conducted (e.g. Heidarzadeh et al. 2008; Okal and Synolakis 2008). Some studies focused on the tsunami hazard assessments for scenarios similar to the 1945 Makran tsunami event (e.g. Heidarzadeh and Satake 2017; Jaiswal, Singh, and Rastogi 2009; Momeni et al. 2020; Neetu et al. 2011) and the 2013 onshore tsunamigenic earthquake in Makran, which triggered a landslide tsunami (Heidarzadeh and Satake 2014). On the other hand, some studies examined hypothetical scenarios based on the geological and geophysical studies of the MSZ (e.g. El-Hussain et al. 2016, 2018; Hoechner, Babeyko, and Zamora 2016; Rashidi et al. 2020). Two studies examined the effect of the rupture of the splay faults on tsunami hazard in the MSZ (Heidarzadeh, Pirooz, and Zaker 2009; Rashidi et al. 2021). Heidarzadeh, Pirooz, and Zaker (2009) studied a single scenario of splay fault rupture accompanying the thrust event on the main subduction interface in the eastern MSZ. Heidarzadeh, Pirooz, and Zaker (2009) considered fixed geometry, location, magnitude, and uniform slip of the splay fault rupture. Recently, Rashidi et al. (2021) performed a tsunami hazard assessment for western MSZ due to a scenario in which ruptures occur only on splay faults without subduction thrust events. Rashidi et al. (2021) used a logic tree approach to perform tsunami hazard assessment considering different scenarios of individual splay fault ruptures or combined splay fault ruptures. They considered fixed length,

location, and uniform slip distribution for each fault. Results of these studies revealed significant impacts of splay fault ruptures on local tsunami hazards. This study presents a more comprehensive and realistic modeling framework of tsunami hazards due to splay faulting for the Makran region as detailed in the following.

The logic tree approach was initially employed for probabilistic seismic hazard assessment (Coppersmith and Youngs 1986). Recently, it was applied to assess tsunami hazard assessment (e.g. Annaka et al. 2007; Fukutani, Suppasri, and Imamura 2015; Horspool et al. 2014; Lorito et al. 2015). This is a practical method for considering multiple alternatives for various uncertainties associated with tsunami hazard assessments. The logic tree approach offers the advantage of its simplicity in selecting source parameters. However, it has limited flexibility to consider alternative hypothetical slip distributions and associated characteristics since the number of branches increases rapidly.

Non-uniform patterns of slip distribution over a fault plane are more realistic than uniform distributions since they reflect the intrinsic complexity of earthquake rupture. The stochastic source modeling approach facilitates the generation of synthetic realizations of realistic source models (Mai and Beroza 2002). As a result, this approach has been used in various tsunami hazard assessments around the world (Fukutani, Suppasri, and Imamura 2015; González et al. 2020; Momeni et al. 2020; Mori et al. 2017; Rashidi et al. 2020; Woessner and Farahani 2020). One of the key elements of the stochastic modeling method is scaling relationships. Goda et al. (2016) proposed scaling relationships of various earthquake source parameters for the stochastic tsunami method. Non-uniform patterns of slip distributions have been neglected in most of the tsunami hazard assessments of the MSZ, apart from two studies of Momeni et al. (2020) and Rashidi et al. (2020). Momeni et al. (2020) used the stochastic slip distribution approach to study the 1945 Makran tsunami event, whereas Rashidi et al. (2020) utilized a similar method to assess the tsunami hazard related to 100 hypothetical rupture sources. The results of Momeni et al. (2020) showed a significant sensitivity of the maximum wave height along the shoreline to the location of the large slip areas on the fault plane. The abovementioned studies on the MSZ considered ruptures only on the main subduction zone interface.

In this study, the effect of splay fault ruptures on tsunami hazard of the eastern Makran shoreline is investigated by developing a framework that utilizes the logic tree and stochastic rupture modeling. Average slip models, which are calculated utilizing numerous stochastic source models, and many configurations of stochastic source models are used in this paper to generate the results. Assessing the effect of

splay fault rupture is necessary to comprehensively evaluate the tsunami hazard for the MSZ. This assessment needs to be conducted using the logic tree and stochastic source method rather than single deterministic models because it enables the results of the assessment and the developed framework to be used in probabilistic tsunami hazard analyses as well. The novelty and significance of this study are that for the first time, a systematic approach of evaluating the effect of splay fault rupture accompanying the plate-boundary rupture is developed using logic tree and stochastic slip models. The adopted approach enables this study to consider the uncertainties of the geometry of the splay fault rupture, seismic moment split ratio, and earthquake slip heterogeneity. Also, the uncertainty of splay fault rupture location is considered by varying the asperity location within the fault plane, noting that asperity refers to an area where the largest slips (e.g. larger than the average slip of the fault) occur. In addition, the most recent published geometry and geological information of the MSZ (Hayes et al. 2018; Penney et al. 2017; Smith 2013) and splay fault interfaces (Mokhtari 2015; Smith et al. 2012) are used, which enable this study to assess the tsunami hazards more accurately.

2. Methodology

2.1. Tsunami source

Heidarzadeh, Pirooz, and Zaker (2009) proposed a tsunami source that consists of a rupture on the plate boundary and a splay fault in the eastern MSZ simultaneously. They used findings from Byrne, Sykes, and Davis (1992) to define the geometry and source parameters of the plate boundary rupture. Regarding the splay fault, they considered a hypothetical fault model guided by the 1946 Nankai and the 1960 Chilean earthquakes and tsunamis assuming that the splay fault branches from the plate boundary (Byrne, Sykes, and Davis 1992; Cummins and Kaneda 2000; Heidarzadeh, Pirooz, and Zaker 2009; Plafker 1972). They studied two scenarios with equal moment magnitudes of 8.6. In the first scenario, 100% of the seismic moment was associated with the plate boundary rupture alone. In the second scenario, the seismic moment of the plate boundary rupture was reduced to 91% of the total seismic moment and therefore 9% of the seismic moment was allocated to the splay fault rupture. On the other hand, the tsunami source model proposed by Rashidi et al. (2021) considered the rupture only on splay faults. They used seismic reflection datasets to identify the geometry and source parameters of the splay faults in western MSZ. They considered fixed length, dip, strike, location, uniform slip distribution on the fault planes, and variable widths for

the splay faults based on empirical equations of Wells and Coppersmith (1994).

2.1.1. Main fault model of the Makran subduction zone

Recently, Hayes et al. (2018) developed the Slab2 global subduction zone model that includes three-dimensional geometry models of major active global subduction zones including the MSZ. It provides the dip, depth, and strike of the subduction interface. To develop the 3D MSZ interface in the Slab2 model, the global distribution of earthquake locations, geodetic control points, and active source seismic data were used. Figure 1a shows the geometry of the Slab2 model for the MSZ.

In terms of seismic activity, the eastern part of the MSZ is significantly more active than the western part. However, Smith (2013) and Penney et al. (2017) suggested that the western part of the MSZ might be locked. Figure 1a shows that the plate boundaries of the MSZ based on the Slab2 model match the seismicity data. Strike-slip, normal, and thrust events with $M_w > 4.5$, that occurred in the MSZ from 1945 to 2017, are obtained from Penney et al. (2017) and are shown in Figure 1a. The boundaries of the MSZ, specified by the Slab2 model, are consistent with the locations of strike-slip events.

Figure 1b shows a generic plate boundary model of the MSZ that is developed to perform the stochastic tsunami simulation. The plate interface of the MSZ model has two segments, that is, the eastern and western segments. The length and width of the source model are 1,080 km and 230 km, respectively. The dip of the subduction interface is a constant value of 8° for the entire MSZ. This value is consistent with the suggested range of dip values by the Slab2 model (Hayes et al. 2018). The top edge of the fault plane reaches the ocean bottom. This is supported by Penney et al. (2017); their work strongly favors shallower trench depths and 0 km is consistent with the current understanding of the subduction zone. Based on Smith et al. (2012) and Penney et al. (2017), the locking depth of the MSZ is 30–35 km.

Figure 1c shows the cross-section A-A' that is indicated by a blue line in Figure 1b. According to the A-A' cross-section, the main MSZ plate interface source model reaches a depth of 30 km with a width of 230 km and a dip angle of 8° . To generate slip values in stochastic source modeling, the MSZ is discretized into $10 \text{ km} \times 10 \text{ km}$ sub-faults. It is important to note that the proposed model is applicable for a comprehensive range of probable events in the MSZ up to megathrust $M_w 9$ earthquakes when the whole rupture is considered. Due to the significantly higher seismic activity of the eastern MSZ compared to

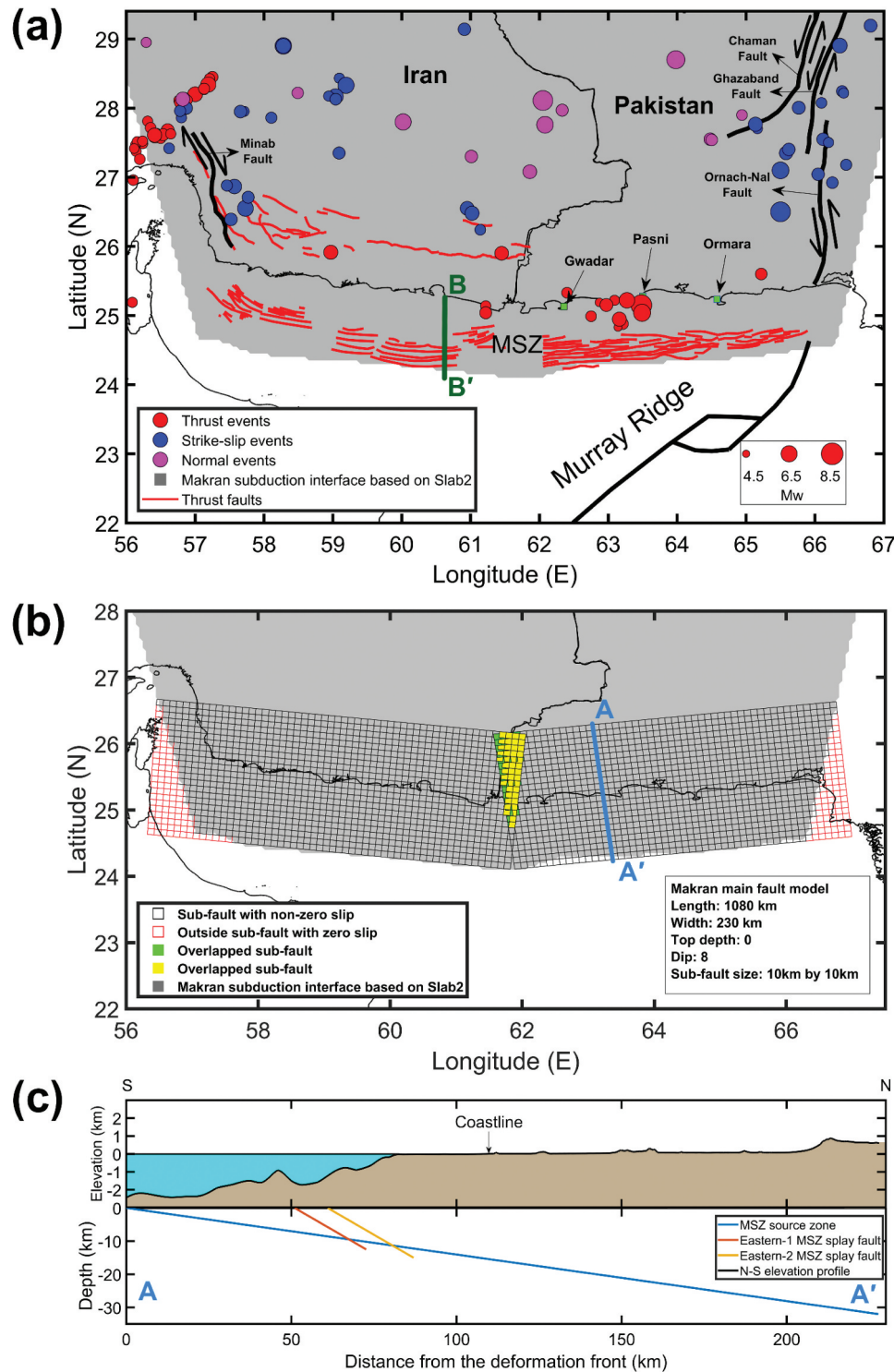


Figure 1. (a) Makran fault plane geometry based on Slab2 and splay fault locations along the Makran, (b) Makran main fault model, and (c) cross-section profile (A-A') of the Makran main and the splay faults models.

the western part, the main focus of this study is the eastern part; therefore, the ruptures on the main plate boundary are generated only for the eastern segment.

2.1.2. Splay faults models of the Makran subduction zone

There are many splay faults in the eastern and western Makran. These faults are identified using seismic reflection data provided by Smith et al. (2012) and Mokhtari

(2015) for eastern Makran and western Makran, respectively. Most of these splay faults are thrust faults that are located near the deformation front (Figure 1a) (Mokhtari 2015; Pajang et al. 2021; Smith et al. 2012). The splay thrust faults may be activated by the rupture on the Makran plate boundary (Kame and Yamashita 1999). It should be noted that the identified splay faults differ in terms of their proximity to the coastline. Some are closer to the coastline and others are farther. The

locations of the identified splay faults are important because the effect of splay faults is local and the closer splay faults to the coastline may pose a greater tsunami risk as compared to the farther ones. Also, the dip angle of the splay faults plays a crucial role in the assessment of tsunami hazard because steeper faults cause greater vertical deformations on the seabed and consequently lead to larger tsunami amplitudes.

Since the main focus of this study is on eastern Makran, only the generic splay fault models of eastern Makran are developed based on the data provided by Smith et al. (2012) and Mokhtari (2015). Four factors are considered. Firstly, the length of the splay fault models is considered to cover the entire shoreline of eastern MSZ. It allows to consider the uncertainty of the location of splay ruptures along the coastline. The strike angles of the splay fault models are similar to the plate boundary ruptures.

The second factor is the proximity of the splay fault models to the shoreline. Although the splay faults that are located near the accretionary front line are more probable to rupture (Kame and Yamashita 1999), several splay faults with different distances to the shoreline and near the accretionary front line are identified (Figure 1a) (Smith et al. 2012), and the possibility of their rupture cannot be excluded. Thus, to consider the uncertainty of the distance between splay fault rupture and coastline, two generic splay fault models are developed with different distances from the shoreline. It is worth mentioning that the locations of the two generic splay fault models (Figure 2) are consistent with the identified splay faults in the region (Figure 1a).

Thirdly, two dip angles of 30° and 40° are considered as two representative cases for the generic splay fault models to account for the uncertainty of dip angle. The dip angle of 30° is consistent with the data provided by Smith et al. (2012). The cross-section profile of the splay faults in western MSZ (Figure 3) shows dip angles of up to 40° (Mokhtari 2015; Pajang et al. 2021). Consideration of two dip values as two representative cases can capture the uncertainty of this parameter. However, for specific splay faults, dip angles could be gentler or steeper. Figure 3 shows the cross-section B–B' that is indicated by a green line in Figure 1a. Although the cross-section profile is related to western MSZ, the dip angle of 40° is deemed applicable to eastern MSZ because of the relative proximity of the cross-section profile to eastern MSZ.

The steeper dip angles for splay faults can significantly affect the tsunami hazard for the nearby regions, and this possibility is taken into account in this study.

The fourth factor is related to the width of the generic splay faults models. The width is defined based on the assumption that the rupture on splay faults can reach up to the seafloor and also ends when it reaches the main MSZ interface (Kame and Yamashita 1999; Park et al. 2002). The location, length, width, strike, and dip values of the generic splay fault models are given in Table 1. Figure 3 shows the generic splay fault models of eastern Makran and Figure 1c shows the cross-section of the developed models (cross-section A–A' – Figure 1b). These developed fault models are a placeholder, and a rupture model (i.e. slips) floats along the strike and dip directions when the rupture area is smaller based on the assumed magnitude.

2.1.3. Earthquake scenarios

In this study, a scenario earthquake magnitude of Mw 8.6 is considered for an earthquake event that can trigger the rupture on the splay faults in eastern Makran. This moment magnitude is the same as the magnitude that was considered by Heidarzadeh, Pirooz, and Zaker (2009), which is based on the maximum possible earthquake in eastern Makran. Since the main focus of this study is on splay fault characteristics, a single value of Mw 8.6 for the main fault is selected to keep the case study less complex and to focus upon the tsunami hazard assessment framework for splay faults. To consider the uncertainty of the ratio of the seismic moment of splay faults to the entire rupture (i.e. combination of plate boundary and splay fault ruptures), three different values of 5%, 10%, and 15% are considered. These values are consistent with the seismic moment split ratio of 9% considered by Heidarzadeh, Pirooz, and Zaker (2009) and with the study of Baba et al. (2006), which assigned 15% of the entire seismic moment to the splay fault rupture. Three different scenarios of earthquake ruptures are studied based on different combinations of ruptures on the plate boundary and splay faults:

- (1) Main plate boundary rupture only: 100% of the entire seismic moment is assigned to the rupture on the plate boundary. This case serves as a benchmark.

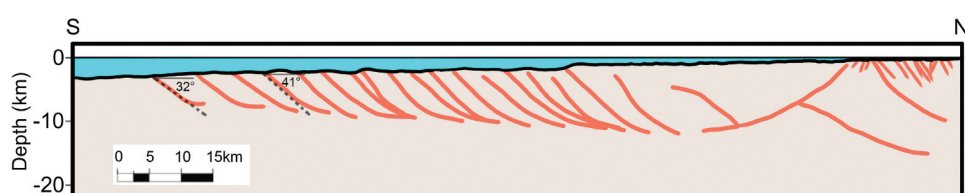


Figure 2. Cross-section profile B–B' (Figure 1a) of the Makran splay faults.

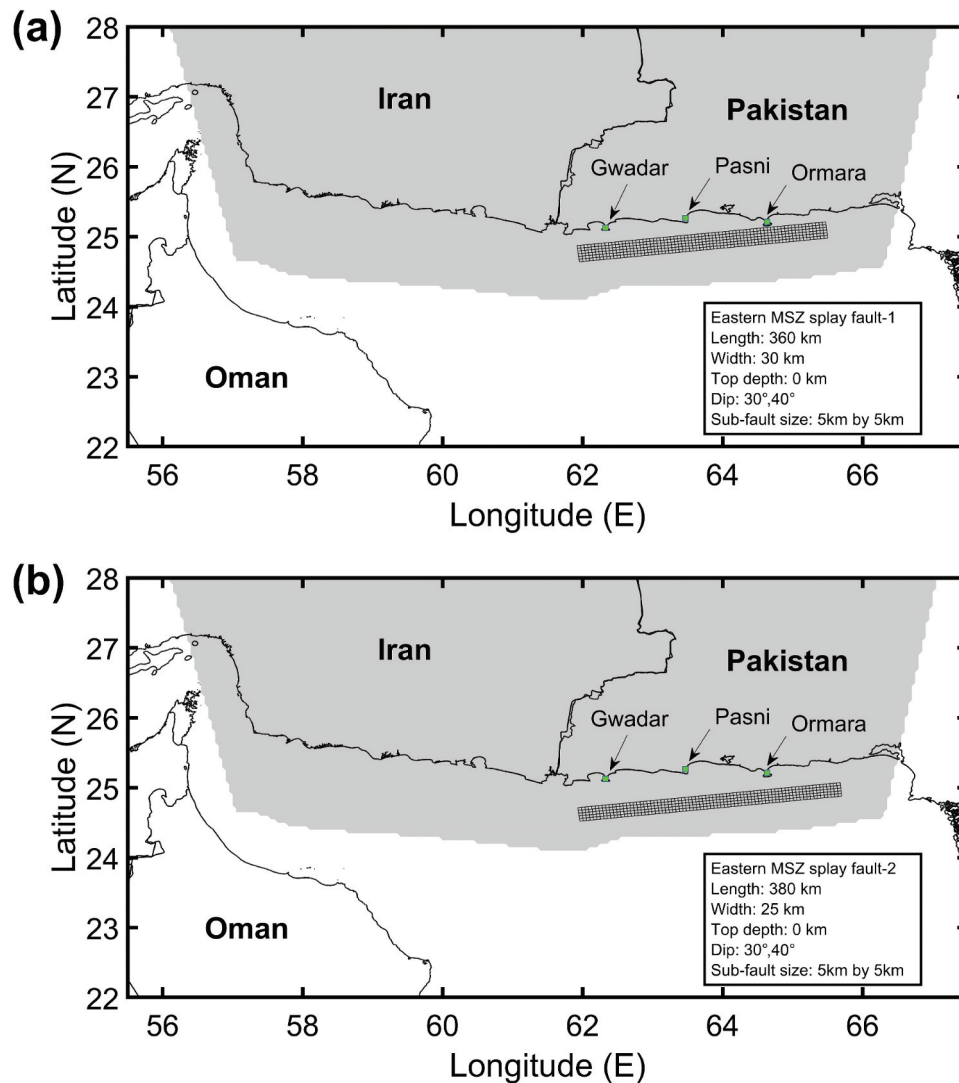


Figure 3. Generic splay faults models of eastern Makran: (a) Splay fault-1 and (b) Splay fault-2.

Table 1. Eastern Makran generic splay faults models.

	Southeast corner	Length (km)	Width (km)	Strike angle	Dip angle
Splay fault-1	N24.88°, E65.70°	360	30	264°	30°, 40°
Splay fault-2	N24.98°, E65.50°	380	25	264°	30°, 40°

- (2) Single-splay fault rupture: Based on the selected value of the seismic moment split ratio, the seismic moment is split into two parts, one for the plate boundary and another for the splay fault. For instance, if the seismic moment split ratio of 10% is selected, 10% of the entire seismic moment is allocated to rupture on a single splay fault plane and the remaining 90% (100% minus seismic moment split ratio) is assigned to the rupture on the plate boundary. Hence, two earthquake sources need to be considered in this scenario, one for the plate boundary rupture and the other for a splay fault rupture.
- (3) Two-splay fault ruptures: According to the chosen value of the seismic moment split ratio, the

seismic moment is split into two parts, one part for the plate boundary and another part for the splay faults. As an example, for the selected value of 10%, 10% of the entire seismic moment is divided into two splay fault ruptures (5% for each splay fault plane), and the remaining 90% is allocated to the rupture on the plate boundary. Thus, it is necessary to consider three earthquake sources in this scenario, one for the plate boundary plane and two for splay faults.

The moment magnitudes of ruptures on the plate boundary and splay faults due to different seismic moment split ratios are given in [Table 2](#).

For each earthquake source, an appropriate fault model is defined (section 2-1-1 and section 2-1-2). For the earthquake sources related to the plate boundary rupture, the fault model introduced in [Figure 1b](#) is used and for the earthquake sources related to splay faults, the fault models introduced in [Figure 2](#) are used. Consequently, the moment magnitude of the earthquake sources is selected from [Table 2](#), depending on

Table 2. Moment magnitudes of ruptures on the plate boundary and splay faults.

Scenario	Seismic moment split ratio	Plate boundary rupture (Mw)	Splay fault rupture (Mw)
Plate boundary rupture only	0%	8.6	N/A
Single-splay fault rupture	5%	8.58	7.73
	10%	8.57	7.93
	15%	8.55	8.05
Two-splay fault rupture	0%	8.57	7.53 + 7.53
	10%	8.57	7.73 + 7.73
	15%	8.55	7.85 + 7.85

the rupture scenario. As an example, for the second scenario and seismic moment split ratio of 10%, the moment magnitudes of the plate boundary and splay fault ruptures are Mw 8.57 and Mw 7.93, respectively. For each earthquake source, the asperity zone and corresponding slip concentration range within the fault model are defined. The asperity zone can be defined as a smaller sub-region in which the slip values of the sub-faults are greater than the average slip value of the earthquake source by a specified threshold (for example 1.5 times the average slip) (Murotani, Satake, and Fujii 2013). In this study, the slip concentration range of the asperities for both plate boundary and splay faults is set to 65–90%. Therefore, between 65 and 90% of the total earthquake slip of the rupture on plate boundary and splay faults should occur within the specified asperity zone, assuming the simulated slip is higher in the defined asperity region.

2.1.4. Asperity zones for main fault sources

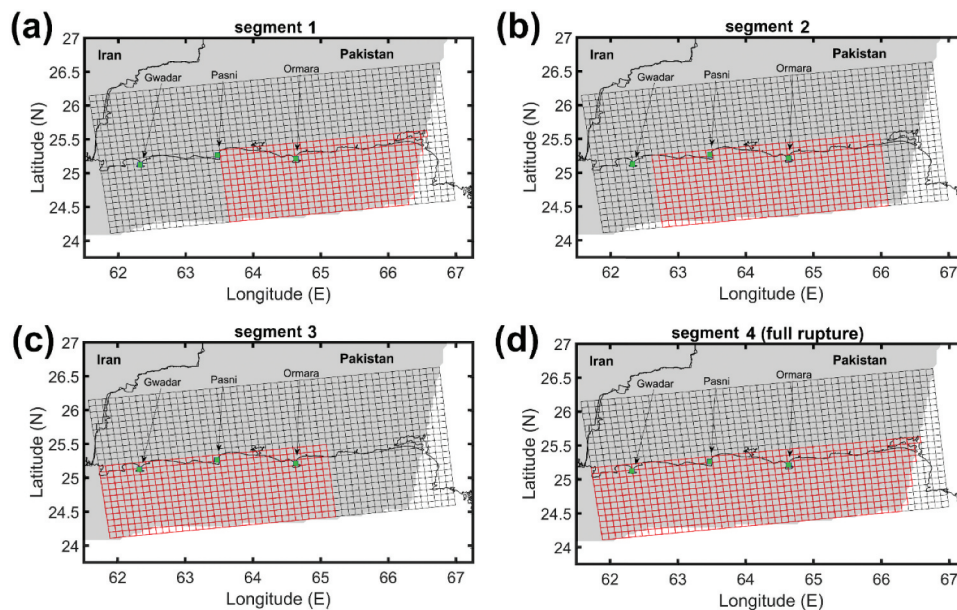
To assess significant tsunami hazard in eastern MSZ, the asperity areas are defined on the top-half of the plate boundary model. The ruptures that occur on the top-half of the plate boundary model are offshore and generate significant deformation on the seafloor. On the other hand, the ruptures that occur on the bottom-half of the plate boundary model (deeper parts) are

onshore and they may not cause a tsunami. To consider the uncertainty of the location of ruptures on the plate boundary model along strike (along the shoreline), four asperity areas are defined on the generic plate boundary model to cover the entire shoreline (Figure 4a-d).

2.1.5. Asperity zones for splay fault sources

To show the effect of splay fault rupture along the eastern Makran shoreline, it is split into different segments. The locations of the splay ruptures can be controlled by specifying the target asperity areas in stochastic sources. Eight asperity areas are defined for the single-splay fault rupture scenario on each of the splay fault models of eastern MSZ (Figure 5a-h). Since the asperity areas on the splay fault-1 and splay fault-2 are similar, Figure 5 shows the asperity areas on the splay fault-2 only. These eight asperity areas cover the entire shoreline of eastern MSZ. In addition, the uncertainty of occurrence of asperities along dip is considered by defining the full-width asperities and top-half asperities on the splay fault models. Ruptures that occur on the top-half of the splay fault models generate greater deformation on the seafloor and they can cause more significant tsunami hazard.

For the two-splay fault rupture scenario, both splay faults rupture. Since the magnitude for this scenario for

**Figure 4.** Four asperity areas of the plate boundary model of eastern MSZ.

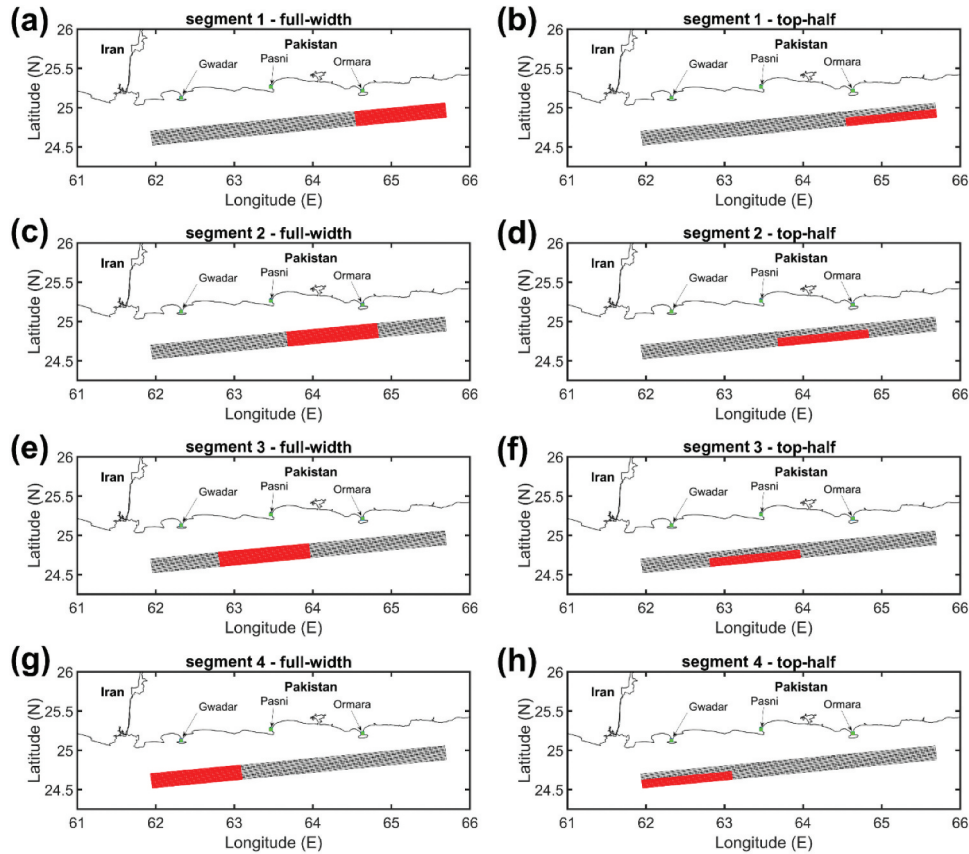


Figure 5. Asperity areas of the splay fault-2 of eastern Makran for the single-splay fault rupture scenario.

each splay fault is smaller (Table 2), the rupture length is shorter. As a result, finer segmentation is needed to cover the same length. Twelve asperity areas for this scenario are defined on each of the splay fault models of eastern MSZ (Figure 6a-l). These 12 asperity areas cover the entire shoreline of eastern MSZ by full-width and top-half asperities.

2.1.6. Generation of stochastic sources and average source models

Once the earthquake scenarios and subsequent earthquake source models are defined, earthquake source parameters must be determined to generate stochastic source models for the plate boundary and splay fault ruptures. In this study, earthquake source parameters are determined using global scaling relationships developed by Goda et al. (2016). Although there are many scaling relationships for earthquake source parameters, those that can be used for generating stochastic source models are not many. The developed relationships by Goda et al. (2016) distinguish tsunamigenic and non-tsunamigenic events. The scaling relationships of Goda et al. (2016) are a practical choice for this study, but this aspect can be explored more widely in the future and alternative scaling relationships by Allen and Hayes (2017) could also be implemented.

Using the SRCMOD database (Mai and Thingbaijam 2014), a number of finite-fault rupture models of past

earthquakes were statistically analyzed by Goda et al. (2016) to develop global scaling relationships. The fault length (L), fault width (W), mean slip (D_a), maximum slip (D_m), correlation length along strike direction (A_z), and correlation length along dip direction (A_x) are evaluated as a function of earthquake magnitude (M_w), whereas the Box-Cox parameter (λ) (Box and Cox 1964) and the Hurst number (H) (Mai and Beroza 2002) are independent of M_w . The aforementioned parameters are further explained below.

The earthquake source parameters indicate the fault plane features in two main categories. The first category relates to the geometry of the fault, which is defined by the fault length, width, strike angle, and dip angle. As for the remaining parameters, they refer to the spatial distribution of slip over the fault plane. Specifically, the mean slip, maximum slip, and Box-Cox parameter are used to model the probability distribution of slip values. Box-Cox parameter is used to make the probability distribution of slip values achieve suitable right-tail characteristics consistent with SRCMOD sources (Box and Cox 1964). While the correlation lengths and the Hurst number are used to model the spatial heterogeneity of the slip values via the von Karman model (Mai and Beroza 2002). Once the earthquake source parameters are generated, they need to be checked to ensure that the generated values are consistent. To do so, the simulated seismic moment ($M_o = \mu W L D_a$, where μ is the rock rigidity

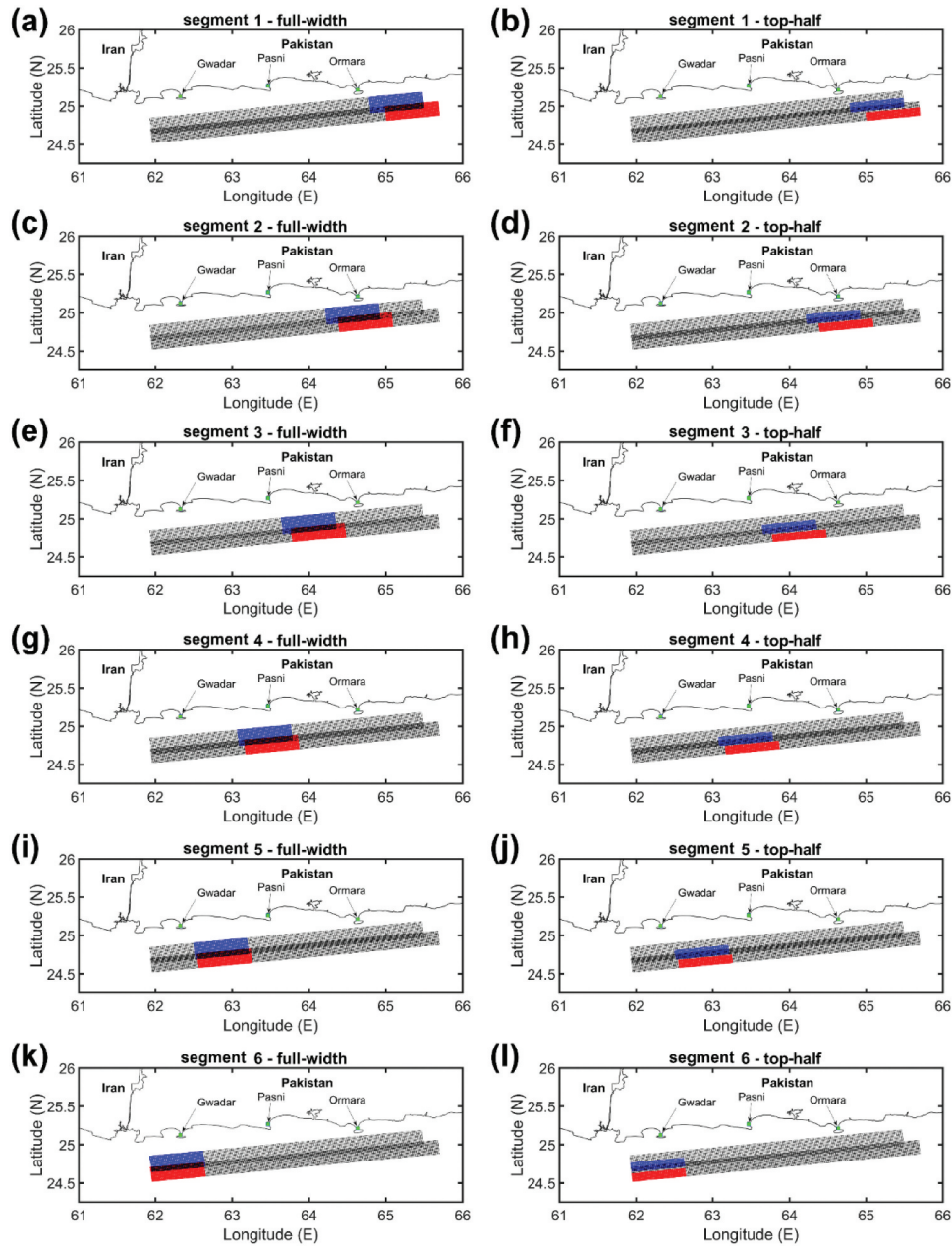


Figure 6. Asperity areas of the splay fault models of eastern Makran for the two-splay fault rupture scenario (Splay fault-1: blue asperity areas, Splay fault-2: Red asperity areas).

$\mu = 3 \times 10^{10} \text{N/m}^2$) is compared to the target seismic moment (defined as the moment magnitude of earthquake source in section 2–1-3). In case the simulated seismic moment does not match the target seismic moment, the values of L , W , and D_a (together with other source parameters) are regenerated until the target magnitude criterion is met.

Following the determination of earthquake source parameters, the slip distribution on the fault plane is generated based on the Fourier integral method (Mai and Beroza 2002). A Box-Cox transformation is then applied to convert the generated random slip field into a slip distribution with realistic positive values. Following the Box-Cox transformation, the slip distribution is modified to avoid very large slip values exceeding the target maximum slip (D_m) and to

achieve the target mean slip (D_a). Finally, the slip distribution is placed randomly within the fault plane. For each earthquake source, the described procedure is repeated until 1000 stochastic source models are generated.

To investigate the effect of different splay fault characteristics (dip, location, and asperity) and seismic moment split ratio and to clearly show the general effect of splay fault rupture along the shoreline, the average slip models are generated by calculating the average slip of each sub-fault using the 1000 slip values of the generated stochastic source models for both the plate boundary and splay faults. Several average source models (seismic moment split ratio of 10%) of plate boundary and splay faults related to different asperities are shown in Figure 7a-h. These average

source models are used to perform tsunami simulations, which are presented in section 3.

2.2. Bathymetry and elevation data

To conduct tsunami simulations, bathymetry, and digital elevation model (DEM) data for the Makran are required. Bathymetry is obtained from the GEBCO-2021 dataset (The General Bathymetric Chart of the Oceans), which includes deep to shallow water regions, with a spatial resolution of 15 arc-sec (GEBCO 2021). The bathymetry data cover the entire Makran including the Iranian-Pakistani nearshore region as well as the coastline of Oman (Figure 8). DEM data are derived from the SRTM (Shuttle Radar Topography Mission) dataset with a spatial resolution

of 1 arc-sec, which includes the onshore topography (USGS 2015).

To develop a nesting grid system of ocean depth and land elevation datasets, three steps are followed. As a first step, bathymetry and DEM datasets (GEBCO-2021 and SRTM) are combined without interpolation. In the generated dataset, grid points are not distributed uniformly because the two datasets have a resolution difference of 15 times (15 arc-sec vs 1 arc-sec). In the second step, only the points derived from the SRTM dataset are used for on-land areas. The third step is to linearly interpolate the composite SRTM (onshore) – GEBCO (offshore) dataset. The nesting grid system for Makran is developed at four levels with a maximum grid size of 810 m and a minimum grid size of 30 m. Grid levels with different resolutions

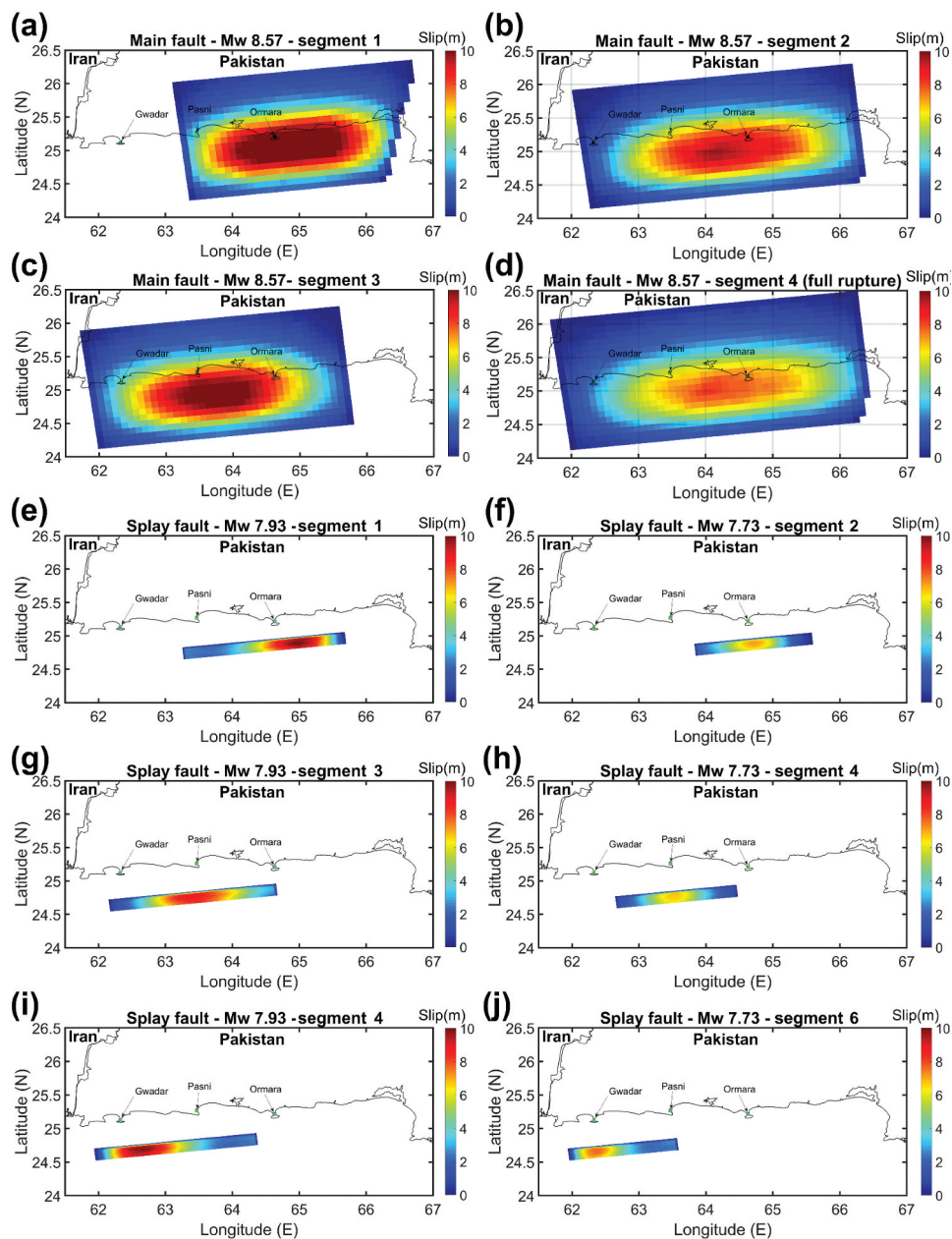


Figure 7. Average source models based on the 1000 stochastic sources (10% seismic moment split ratio) for each earthquake source.

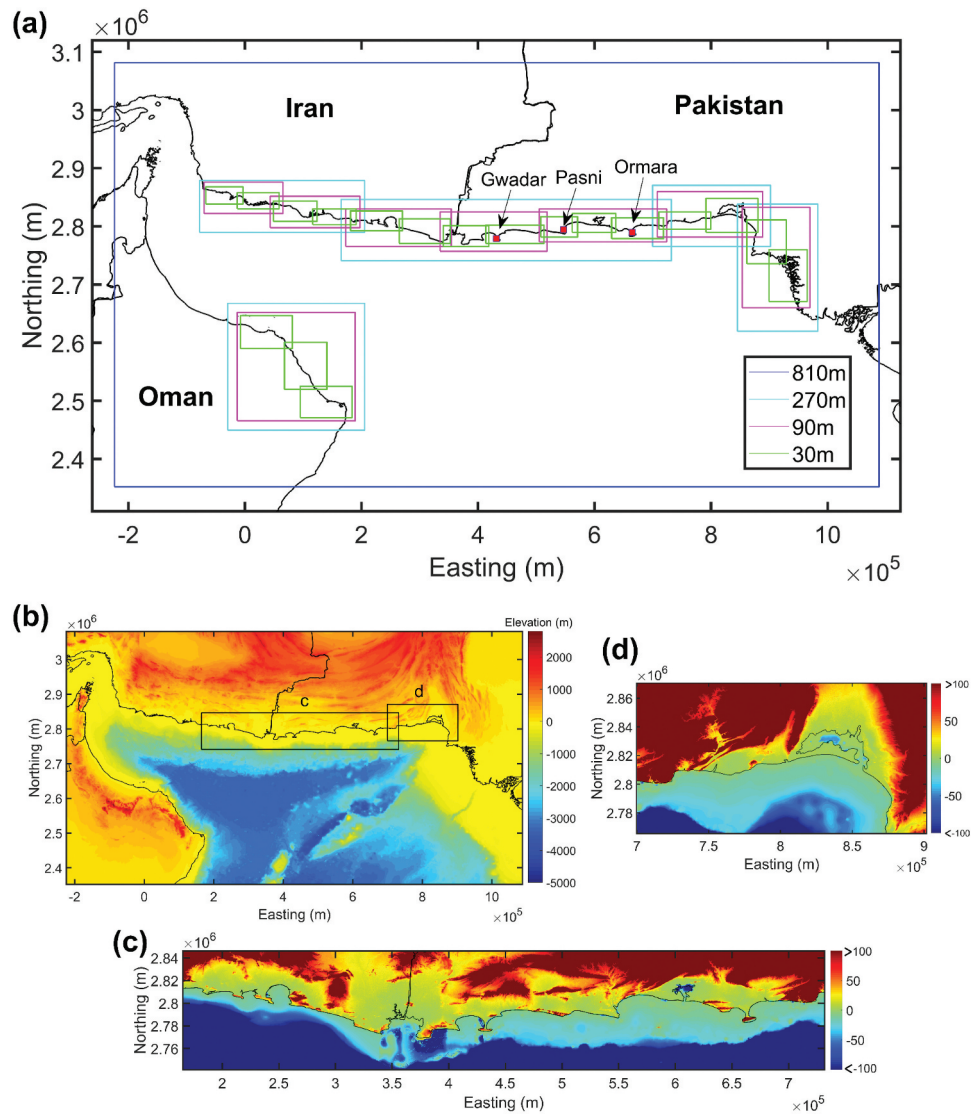


Figure 8. (a) Tsunami computational domain with grid resolutions of 810 m, 270 m, 90 m, and 30 m (identified by colored boxes). Bathymetry and DEM data for: (b) 810 m region, (c) 270 m region around Gwadar and Pasni, and (d) 270 m region around Ormara.

are linked by a factor of 3. The entire area of the MSZ is covered by the 810-m grid. Five 270-m grids, eight 90-m grids, and eighteen 30-m grids are defined within the entire global 810-m main grid (Figure 8a). The results of this study are generated using the 270-m grid. However, the nesting grid system of this tsunami simulation model is developed comprehensively with a minimum grid size of 30 m to be used in future studies without the need for significant modification.

2.3. Stochastic tsunami simulation

The modeling of tsunami propagation and coastal amplification is based on the numerical code developed by Goto et al. (1997). The governing equations of the developed code are Shallow Water Equations (SWEs). Because of the fractional depth of the water in comparison with the tsunami wavelength (i.e. 10 to 500 km), it is possible to approximate tsunami wave propagation using SWEs. Shallow Water theory assumes that water particles have no vertical

acceleration and have a horizontal velocity, which is vertically uniform (Goto et al. 1997; Satake 1995). In this code, offshore tsunami propagation can be simulated from a source region to coastal areas as well as inundation and run-up onshore by solving nonlinear SWEs based on a leap-frog staggered grid systems and applying the Finite Difference method.

To obtain the tsunami simulation results for the eastern Makran shoreline, crustal deformations due to fault ruptures are computed on the 810-m grid using the Okada and Tanioka-Satake equations (Okada 1985; Tanioka and Satake 1996). To calculate the maximum tsunami wave height results along the Pakistan coastlines, the 270-m grid and a time step of 1.0 s are employed. The simulation time step is defined by satisfying the Courant-Friedrichs-Lewy criterion (Courant, Friedrichs, and Lewy 1967). Each simulation is conducted for a total simulation time of 3 hours in the above-mentioned area, without taking into account tidal variation. To account for the bottom friction effect on tsunami waves, Manning's formula is

used with a uniform roughness coefficient of $0.025 \text{ m}^{-1/3}$ s in all cases.

In modeling of the splay fault rupture stochastically, a wide range of parameters and their uncertainties are considered initially. These include dip, location, asperity, seismic moment split ratio, and slip distribution of the main and splay fault ruptures. For each configuration of the main fault rupture and the splay fault rupture, heterogeneous slips are considered through the stochastic source modeling approach. The proposed computational framework can address both types of tsunami source uncertainties. In summary, a list of epistemic and aleatory uncertainties that are considered in this study is presented in Table 3. Figure 9 shows a logic tree of the parameter combinations that are considered in this study.

The parameter space that is needed to be covered is large; given that each tsunami simulation requires several hours of simulation run time per source and large storage space, the calculation cases are necessary to be carefully selected. For instance, for the parameter combination that is considered in this study (i.e. 484) and 1,000 stochastic sources per calculation case, it will be 484,000. For this reason, the whole investigation is split into two parts. First, average slip models are generated and the results due to their ruptures are investigated. For each coastal part of eastern Makran, the ruptures on the segments of the plate boundary and splay faults that are directly located in front of that part of the shoreline are considered (sections 2-1-4 and 2-1-5). Tsunami simulations are conducted for each earthquake scenario (section 2-1-3) by using the average source models which are explained in section 2-1-6. After that, the tsunami wave height results along the eastern MSZ coastline are calculated for each scenario (section 2-3). The main reason for adopting average slip models in the first stage is that while the number of calculations is decreased from 484,000 to 484, the effects of rupture of splay faults as well as their

different characteristics (dip, location, and asperity) can be investigated in an average sense and thus allow to identify the most critical parameters within those varied. The drawback of using the average slip models is that a full impact of uncertain tsunami sources in terms of earthquake slip heterogeneity is not captured thus the predicted maximum wave heights are not the maximum ones. In the second part, several critical configurations of the main fault rupture and splay fault rupture are selected based on the findings of the first part (not the whole combinations of the main fault rupture and splay fault rupture), and for these cases, a complete set of tsunami simulations using the stochastic sources (1000 calculations per case) is conducted. In the second part, the effect of earthquake slip heterogeneity is investigated.

It is worth mentioning that as an improvement to the conventional logic tree method that has been used in early PTHA studies, in this paper, the logic tree paired with the stochastic modeling approach facilitates the consideration of a large number of hypothetical slip distributions. The stochastic tsunami simulation method, that is used in this study, can be broken down into two main parts. Multiple earthquake sources are created in the first part, which is explained in section 2-1, and tsunami simulations are conducted in the second part (section 2-3). Figure 10 shows the flowchart of Part 1 (generating earthquake sources), whereas Figure 11 presents a graphical flowchart of the entire procedure.

3. Results and discussion

The results of this study are presented in two sections: average sources and stochastic sources. In the average sources section, whole combinations of different parameters including plate boundary fault location, splay fault characteristics (dip, location, and asperity), and different seismic moment split ratios are comprehensively studied using average slip models. Key parameters of the splay faults are identified in the first section. Then, in the stochastic sources section, several configurations of the plate boundary fault rupture and splay fault rupture are investigated by using the stochastic sources to consider the earthquake slip heterogeneity. The tsunami simulation results of this paper are generated in the form of maximum wave height of tsunami along the coastline as well as maximum wave height over the entire sea surface area of eastern MSZ, where the wave height is defined with respect to the reference mean sea level.

The main focus of this paper is to quantify the variability of maximum tsunami height along the shoreline of eastern MSZ. The maximum wave heights are calculated at 906 locations along the shoreline with a horizontal spacing of 1 km and at water depths of approximately 10 m. Since the high-quality local

Table 3. Uncertainties considered in the framework.

Type of uncertainty	Uncertainty	Incorporating method
Epistemic uncertainties	Splay rupture scenarios (section 2-1-3)	Logic tree
	Seismic moment split ratio (section 2-1-3)	
	Splay fault planes (section 2-1-2)	
	Splay fault dip angles (section 2-1-2)	
	Segments (sections 2-1-4 and 2-1-5)	
Aleatory uncertainties	Asperity locations along with the dip angles (section 2-1-5)	Stochastic sources and average slip models (section 2-1-6)
	Width and length of earthquake sources (section 2-1-6)	
	Slip distribution (section 2-1-6)	

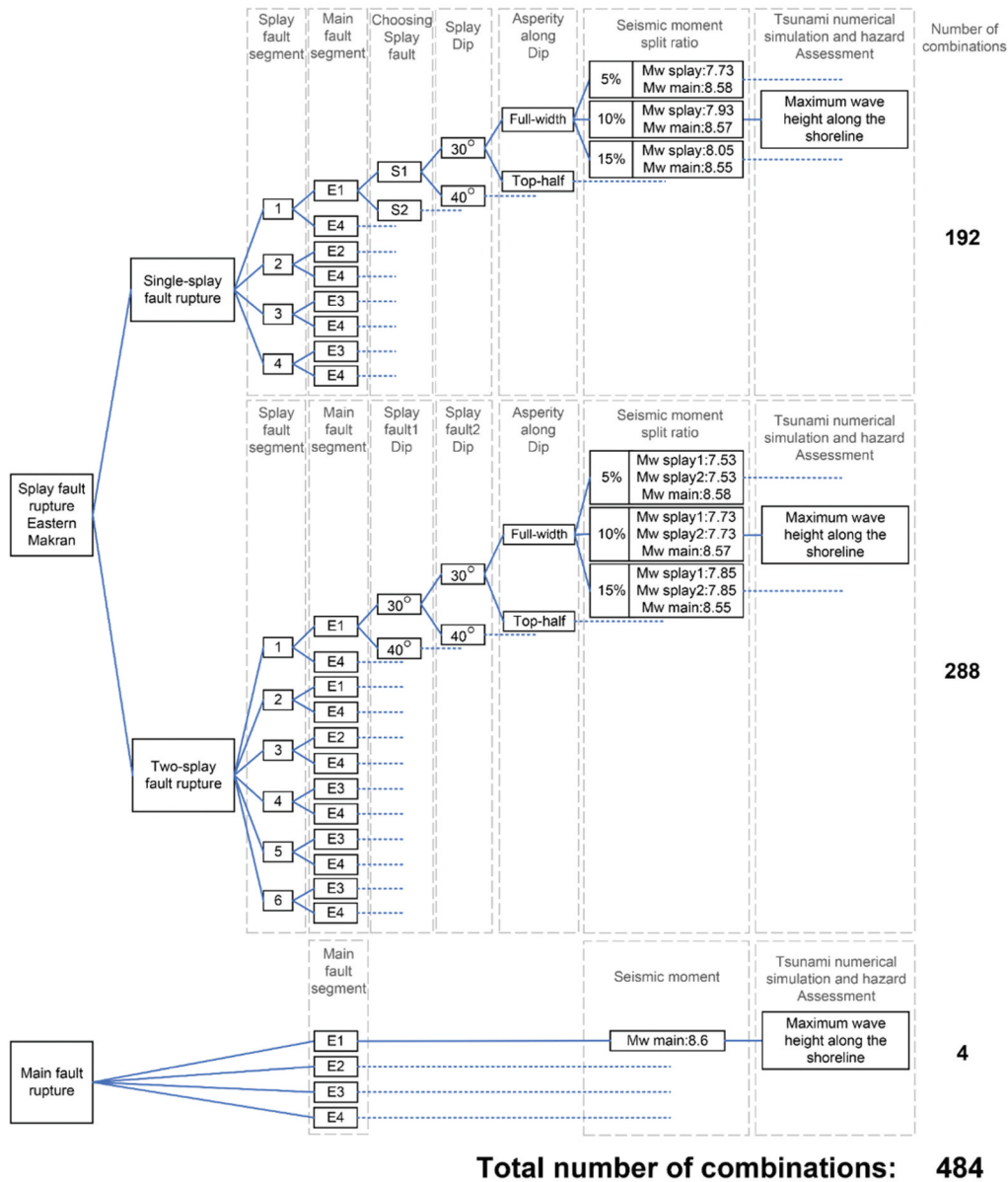


Figure 9. Logic tree of the parameter combinations of tsunami simulations performed in this study.

bathymetry data are not available for this region, 10 m of water depth is chosen to avoid misleading results due to possible errors of the GEBCO dataset in shallower water depths (depth < 10 m). Since the effects of splay faults are local and only eastern MSZ ruptures are considered in this study, the results are mainly presented for the Pakistan shoreline (61.5°E – 66°E).

Three main cities are located on the shoreline of Pakistan: Gwadar, Pasni, and Ormara (Figure 1a). The maximum wave height results for the single-splay and two-splay fault ruptures are generated by focusing on the segments that affect these cities the most. These segments are the ones that are located in front of the cities (Table 4). Several average source models for these segments are shown in Figure 7. In addition to the maximum wave heights, the wave height amplification factors (A) are determined for each segment using the following equation:

$$A = \frac{H_1}{H_0} \quad (1)$$

where H_1 is the wave amplitude due to the combined rupture on the plate boundary and splay fault and H_0 is the wave amplitude due to the plate boundary rupture.

3.1. Average sources

For each segment in a specified scenario of single-splay or two-splay fault ruptures and specified seismic moment split ratio, tsunami simulations for 16 different combinations of rupture of the plate boundary and splay faults are conducted. These combinations are based on different plate boundary fault locations, splay fault planes, their respective dip angles, and asperities along the dip direction (more information is provided in Figure 9). The maximum wave heights

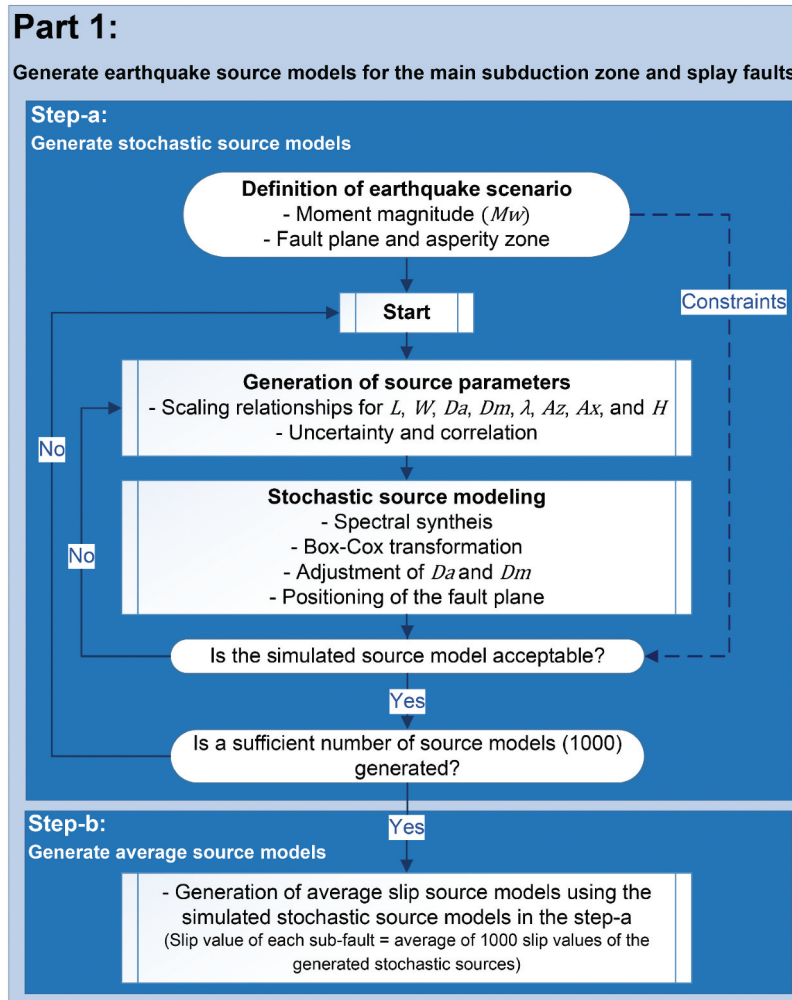


Figure 10. Flowchart of Part 1: Generating earthquake sources.

and amplifications for all combinations and their mean values for the 10% seismic moment split ratio are presented in Figures 12–15. To investigate the effect of plate boundary fault location and individual splay fault characteristics, only the results for the 10% seismic moment split ratio are studied in sections 3-1-1 to 3-1-3. The effects of different seismic moment split ratios (i.e. 5% and 15%) are analyzed in section 3–1-4.

3.1.1. Maximum wave height results

Based on Table 4, the results for the single-splay fault scenario are presented for segment 1 (Figure 5a-b), segment 3 (Figure 5e-f), and segment 4 (Figure 5g-h). Also, the segments that affect the important cities of Gwadar, Pasni, and Ormara the most in the two-splay fault rupture scenario are segment 2 (Figure 6c-d), segment 4 (Figure 6g-h), and segment 6 (Figure 6k-l). The maximum wave heights and amplifications for single-splay and two-splay fault rupture scenarios are presented in Figures 12–13 and Figures 14–15, respectively. For each segment, the splay fault rupture is triggered by two plate boundary rupture asperities. The first one is selected among asperities 1, 2, and 3,

based on the proximity of the segment to them. Asperities 1, 2, and 3 cover the eastern part, central part, and western part of eastern MSZ, respectively (Figure 4a-c). The second one is the full rupture asperity (Figure 4d). The plate boundary rupture asperities are indicated by E1, E2, E3, and E4 (full rupture) hereafter. For example, since segment 1 is located in the eastern part of eastern MSZ, the splay rupture on that segment is triggered by E1 (Figure 4a) and E4 (Figure 4d). In Figures 12 to 15, dashed lines are related to the ruptures that are triggered by the full rupture of the plate boundary fault (E4).

Based on the presented results for both single-splay and two-splay fault scenarios (Figures 12 to 15), significant wave height amplifications occur for the shoreline areas in front of the segments. The maximum wave heights due to the rupture of splay faults reach 8.5 m and 7.0 m for single-splay and two-splay fault rupture scenarios, respectively. For the single-splay fault scenario, the amplification values in the affected areas of segments 1 and 3 are around 2.5, while the amplification for segment 4 is around 4.0. Regarding the two-splay fault rupture scenario, amplifications for

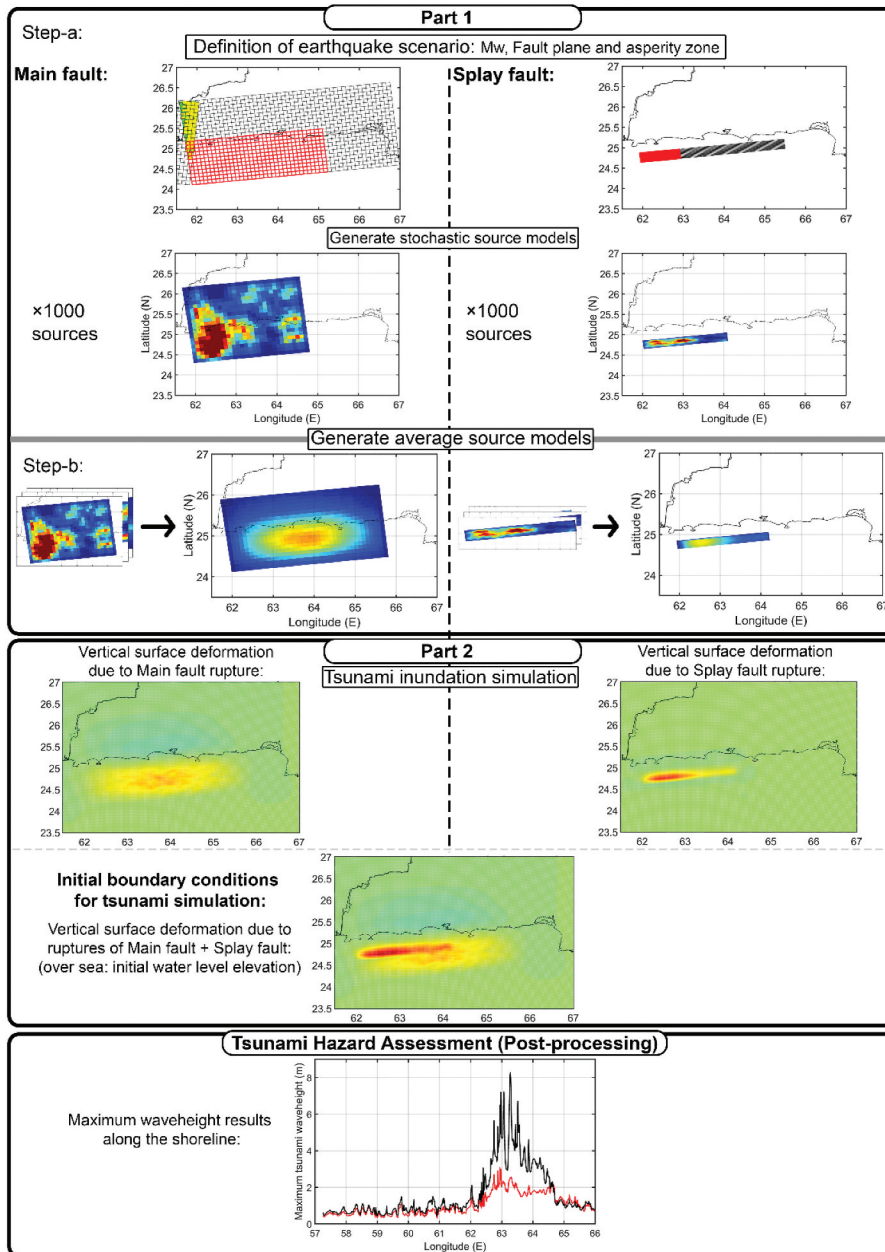


Figure 11. Graphical flowchart of stochastic tsunami simulation method using average sources.

Table 4. The most influential segments of splay fault rupture scenarios for three main cities of Pakistan shoreline.

	Single-splay fault rupture	Two-splay fault rupture
Ormara	Segment 1 (Figure 5a-b)	Segment 2 (Figure 6c-d)
Pasni	Segment 3 (Figure 5e-f)	Segment 4 (Figure 6g-h)
Gwadar	Segment 4 (Figure 5g-h)	Segment 6 (Figure 6k-l)

segments 2, 4, and 6 are around 2.0, 2.0, and 3.5, respectively. The gray lines in Figures 12 to 15 represent the results for 16 splay rupture cases for each segment. The variability among the results is due to the plate boundary rupture that triggers the splay fault rupture, and the individual splay fault characteristics, such as location, dip angle (30° or 40°), and asperity along dip (full-width or top-half) (see Figure 9 for more information). Also, the single-splay fault rupture cases

show much significant variability compared to the two-splay fault rupture cases. The effects of the plate boundary and individual fault characteristics are discussed in more detail in sections 3-1-2 and 3-1-3, respectively.

3.1.2. Effect of plate boundary fault location

The wave height amplifications for the segments that are located in front of Gwadar (segment 4 in single-splay rupture and segment 6 in two-splay rupture) are significantly higher than those from other segments (Figures 12 to 15). This significant difference is caused by the location of the plate boundary rupture that enables the splay ruptures for each segment. Since the initial sea surface displacement, which is the initial boundary condition for tsunami simulation, is

generated by the superposition of the sea surface displacement due to the splay fault and plate boundary ruptures, the maximum wave height results are partly due to the plate boundary rupture and partly due to the splay fault rupture. Figure 16 shows the maximum wave height over the near-shore areas of eastern MSZ due to the single-splay fault rupture scenario (combination of the plate boundary and splay fault ruptures) (Figure 16b,d,f,h) and the ruptures of the plate boundary that triggers them (Figure 16a,c,e,g). Based on Figure 16 and Figures 12 to 15, the coastal areas that are in front of high slip areas, generally experience greater wave heights compared to the remaining parts of the shoreline.

The effect of high slips of the plate boundary rupture for segments 3 and 4 (Figure 16c, e) are similar

(both E3), but the Gwadar shoreline is not located in front of high slips of the plate boundary rupture because Gwadar is located near the westernmost boundary of eastern MSZ. As a result, the maximum wave heights caused by the plate boundary rupture for the Gwadar shoreline are generally lower than the results for the Pasni shoreline (red lines in Figure 12c-d). On the other hand, the effect of splay fault ruptures for segments 3 and 4 are about the same because the amounts of slip are similar and both of them are directly located in front of Pasni and Gwadar. In other words, the maximum wave heights on the Gwadar shoreline (segment 4, Figure 16e,f) are more dependent on the splay fault ruptures compared to the Pasni shoreline (segment 3, Figure 16c,d). As a result, since the effect of splay fault ruptures is about the same for

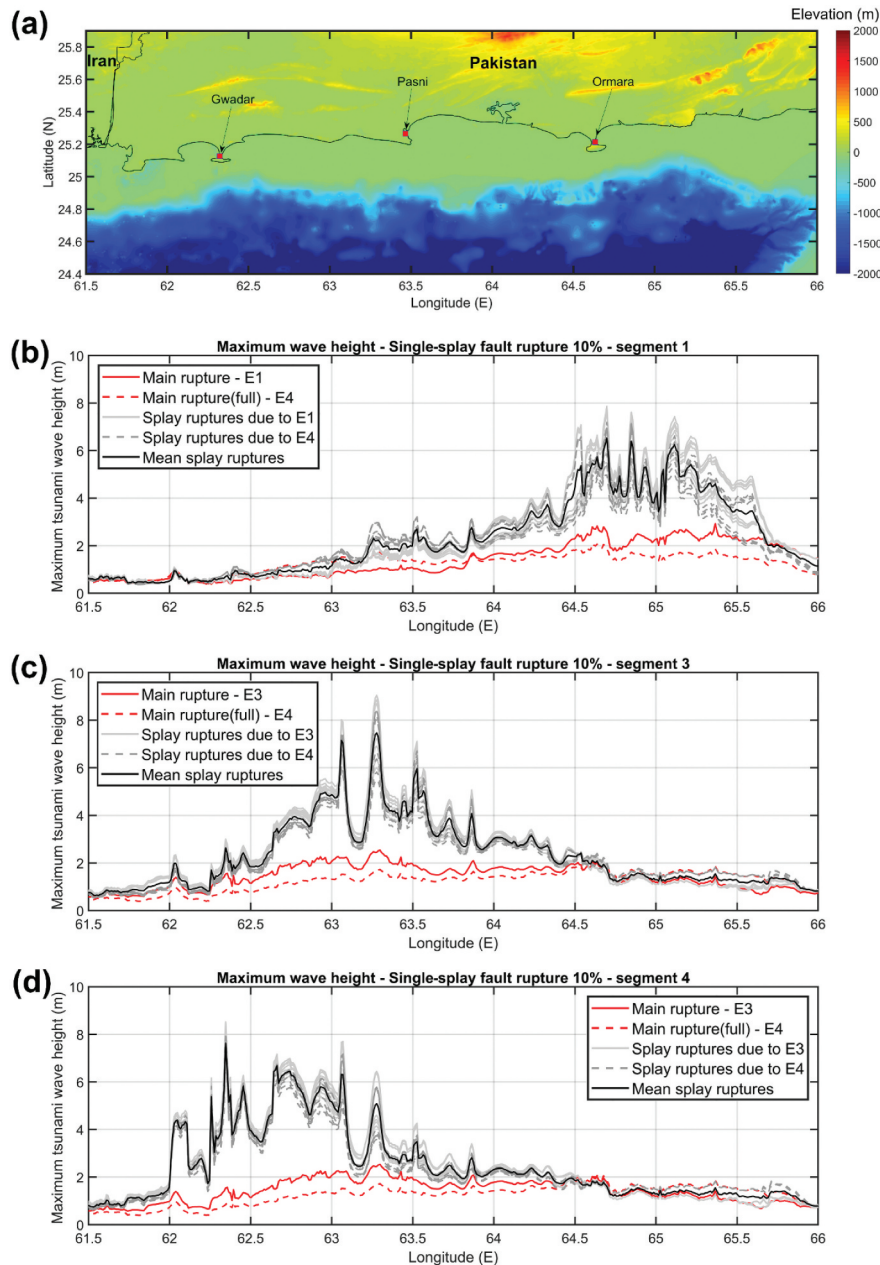


Figure 12. The maximum wave height results of single-splay fault rupture scenario.

both segments 3 and 4 and the plate boundary rupture effect is significantly reduced for segment 4 compared to segment 3, the amplification results for segment 4 are much greater than the amplification results for segment 3 (2.5 vs 4.0) (Figure 13c-d). This reasoning also applies to the two-splay fault rupture scenario because the plate boundary rupture that enables the splay rupture in segment 6 is also E3 (Figure 4c).

The amplification results (Figures 13 and 15) due to the ruptures that are triggered by the full rupture of the plate boundary fault (E4) are significantly greater than the ruptures that are triggered by E1, E2, and E3, while the opposite trend is observed in the maximum wave heights. The maximum wave heights due to the full rupture of the plate boundary fault are slightly lower than the maximum wave heights due to the ruptures triggered by E1, E2, and E3. Hence, it clearly

shows that for the affected areas, the splay fault ruptures are more critical than the plate boundary ruptures for the maximum wave height because splay faults are steeper and are located closer to the shoreline.

3.1.3. Effects of individual splay fault characteristics

Variability among the tsunami simulation results is affected by the plate boundary fault rupture that triggers the splay rupture, and the splay fault characteristics. The effect of the plate boundary fault rupture is explained in section 3-1-2, while the effects of splay fault characteristics are studied in this section.

To analyze the effect of splay fault characteristics, the maximum wave heights of the single-splay fault

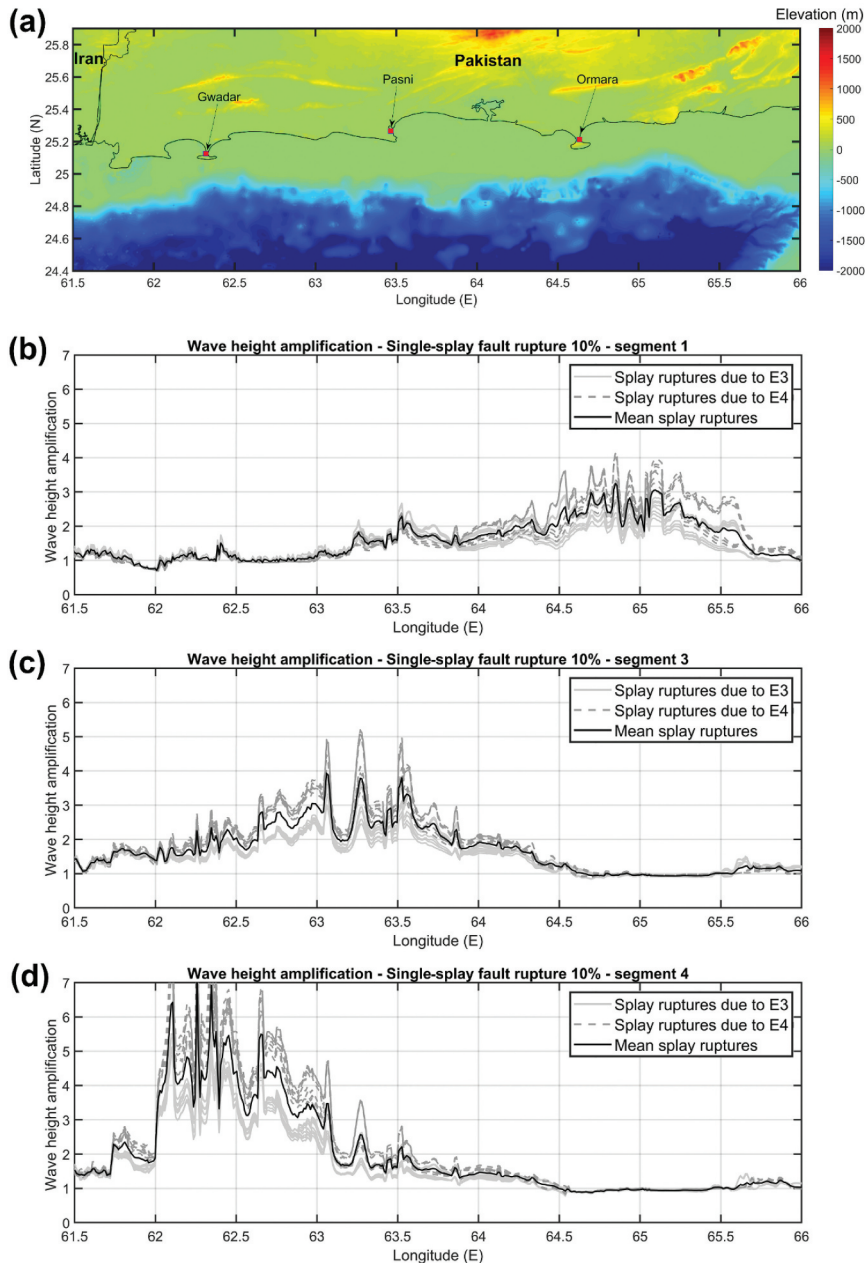


Figure 13. The wave height amplification results (parameter A in Equation 1) of single-splay fault rupture scenario.

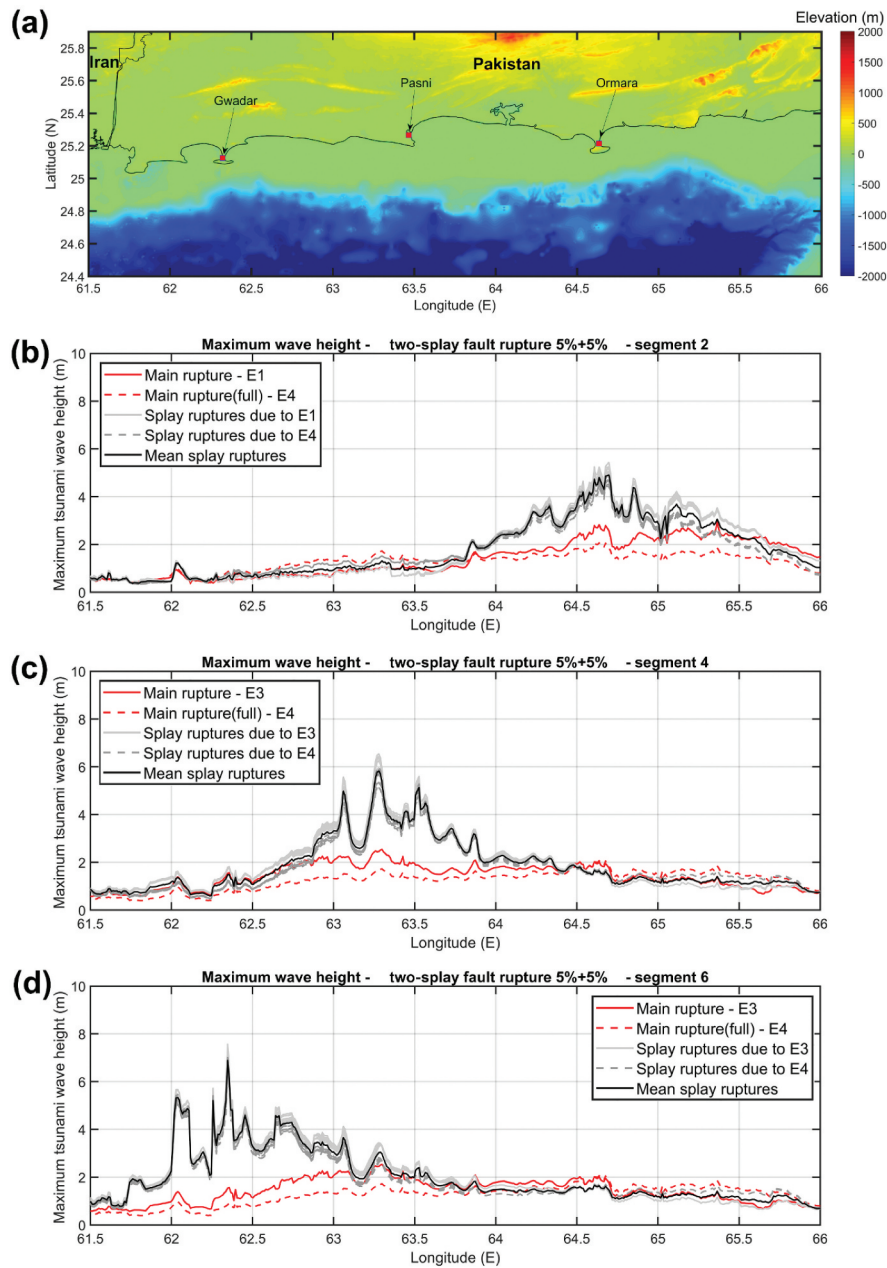


Figure 14. The maximum wave height results of two-splay fault rupture scenario.

rupture scenario for the most affected coastal areas of segments 1, 3, and 4 are presented in Figure 17. To exclude the effect of the plate boundary fault rupture, the maximum wave heights due to the full rupture of the plate boundary fault (E4) are not presented in this section. Figure 17 shows that among splay fault characteristics, the location of the splay faults is the most critical factor. Generally, the results of the splay fault-2, which is located closer to the trench line (Figure 3), are greater than the results due to the splay fault-1. The reason for, that is, the vertical seabed deformation due to the rupture of main + splay fault-2 is greater than main + splay fault-1. Figure 18(a,b) show the spatial distribution of the vertical seabed deformation due to the rupture of E1 + splay fault-1 and splay fault-2 (segment 1, dip 40, top-half asperity). The vertical seabed deformation results from the superposition of

deformations due to main and splay faults. The vertical deformations due to splay fault-2 (red area in Figure 18b) are spatially distributed in an area where the vertical deformations due to the main fault are relatively close to the maximum. As a result, the effects of rupture of both main and splay faults become large in this case. On the other hand, the vertical deformations due to splay fault-1 (red area in Figure 18a) are located more toward the shoreline. Figure 18c shows the cross-section (B–B') (Figure 18a-b) of the seabed deformation due to the aforementioned cases. This cross-section (B–B') also shows the difference between the seabed deformation due to the two cases. In other words, the critical factor is the coincidence of locations of high slip areas on the main fault and splay fault. If they occur coincidentally, the maximum wave heights become significantly greater. The effects of dip angles

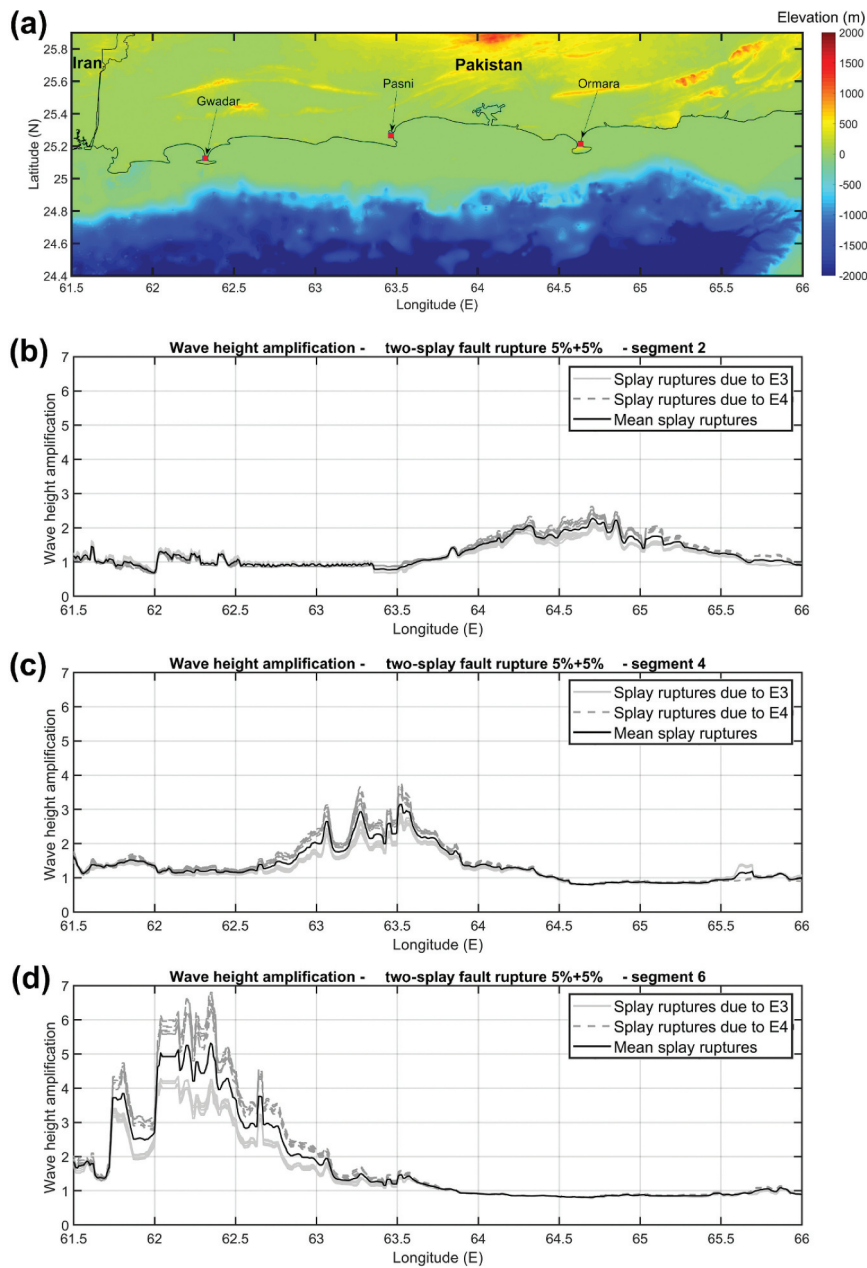


Figure 15. The wave height amplification results (parameter A in Equation 1) of two-splay fault rupture scenario.

and asperities are approximately similar. Among the splay fault ruptures that are located on the same splay fault plane, the ruptures that experience top-half asperities mostly generate greater tsunami heights compared to full-width asperities (Figure 5).

Finally, among the splay ruptures that are located on the same splay fault plane and experience the same asperity, tsunami heights from the ruptures due to a steeper dip angle (40°) are generally larger than those of the ruptures due to a 30° dip angle. As an example, all of these three factors are analyzed for a specific point at 63.55°E (Figure 17b). At this location, all of the wave height results due to splay fault-2 are larger than those due to splay fault-1; the average of maximum wave heights due to splay fault-2 is 20% higher than that due to splay fault-1. For the results due to splay fault-1, solid black and red lines

(Figure 17b) are above the dashed lines which means the greater influence of the effect of asperities over the effect of dip angle. The average of the heights due to top-half asperity rupture is around 7% greater than that due to full-width asperity rupture. Also, the average of the results due to a steeper dip angle (40°) is 4% greater than that due to a 30° dip angle.

The variability for the single-splay fault rupture results is significantly greater than that for the two-splay fault rupture cases because, in the latter, the ruptures occur on both splay fault-1 and splay fault-2. In other words, the effect of location, which has been identified as the most critical factor of splay fault characteristics, does not make differences between the cases of the two-splay fault rupture scenario.

The maximum wave heights show that the effect of location significantly decreases for segment 4

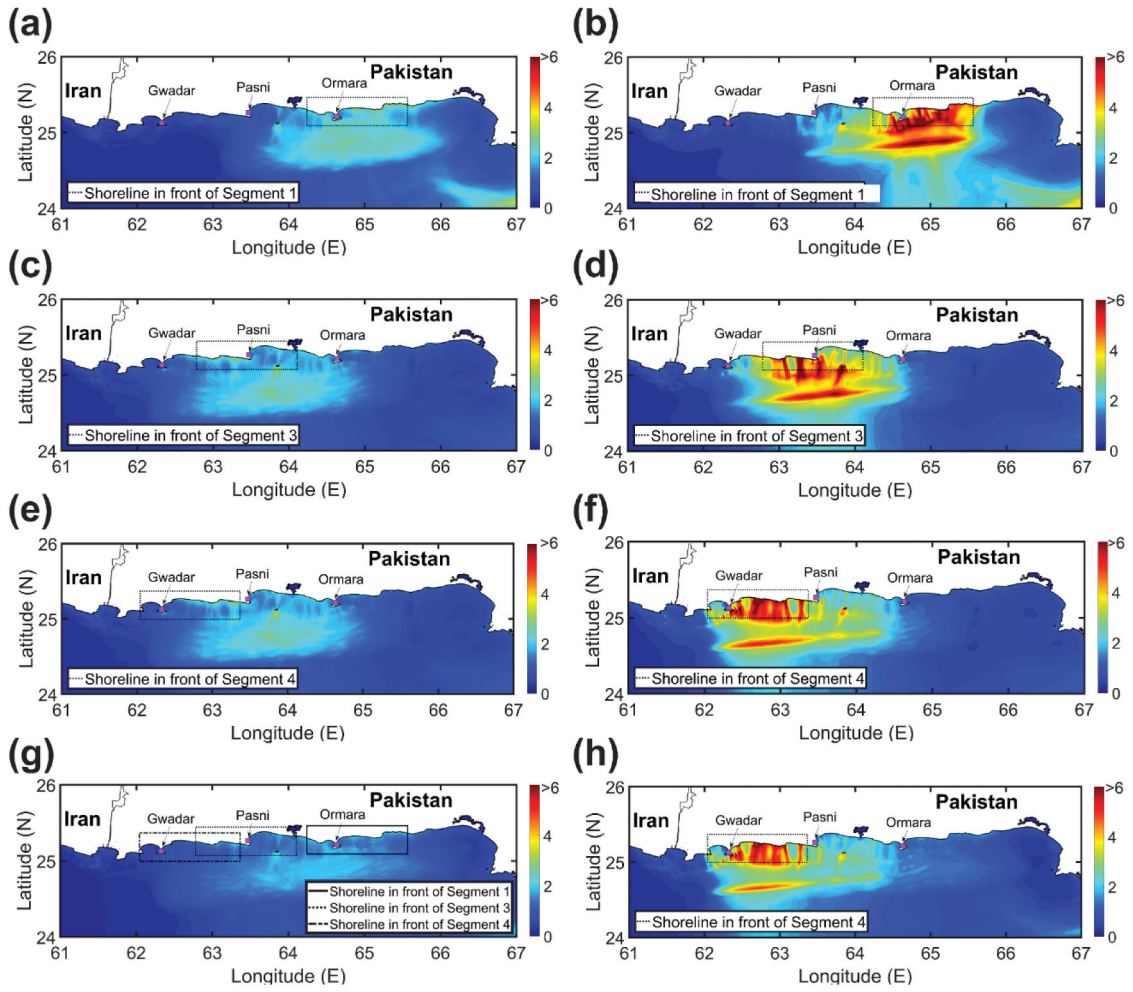


Figure 16. Maximum wave height over the near-shore areas of eastern MSZ for the single-splay fault rupture scenario (10% seismic moment split ratio) due to the: (a) plate boundary fault rupture of E1, (b) combination of plate boundary (E1) and splay fault ruptures for segment 1, (c) plate boundary fault rupture of E3, (d) combination of plate boundary (E3) and splay fault ruptures for segment 3, (e) plate boundary fault rupture of E3, (f) combination of plate boundary (E3) and splay fault ruptures for segment 4, (g) plate boundary fault rupture of E4 (full rupture), (h) combination of plate boundary (full rupture – E4) and splay fault ruptures for segment 4.

compared to segments 1 and 3. As it is already mentioned in section 3–1–2, the plate boundary rupture effect is significantly reduced for segment 4 compared to segments 1 and 3. On the other hand, the vertical deformations due to the rupture on splay faults are about the same for all segments. Therefore, in segment 4, the locations of high slip areas for both splay fault-1 and splay fault-2 do not coincide with the locations of high slip areas for the main fault (E3) and the difference between the two cases is less significant than the segments 1 and 3. In other words, the results due to ruptures on splay fault-1 and splay fault-2 for segment 4 (red-black vs magenta-blue lines in Figure 17c) are more similar compared to segment 1 (red-black vs magenta-blue lines in Figure 17a).

Although the effect of splay fault planes (splay fault-1 vs splay fault-2) generally increases eastward, some parts of the shoreline, such as the coastal segment 63.1E°–63.2E° in Figure 17b, show significantly lower variations between different cases of splay fault ruptures in terms of maximum wave heights and

amplifications compared to adjacent shoreline areas (e.g. coastal segments 63.0E°–63.1E° and 63.2E°–63.3E°). In addition to the source characteristics, the wave amplitudes are affected by large-scale bathymetry features along the coast as well. Wave shoaling and focusing are caused by these features. Figure 19 shows the bathymetry data and maximum wave heights (due to the single-splay fault rupture scenario of the splay fault-2) over the areas around 63.1E°–63.2E°, which is indicated by the dashed rectangle. Figure 19a shows a significant increase in the water depths (more than 30 m) compared to the adjacent areas and Figure 19b shows a substantial drop in the maximum surface elevation height due to the tsunami. As a result, the significant increase in the water depths in that area results in lower variations between different cases of splay fault ruptures compared to the adjacent areas.

3.1.4. Effect of seismic moment split ratio

The effect of 5%, 10%, and 15% seismic moment split ratios on the tsunami simulation results is investigated.

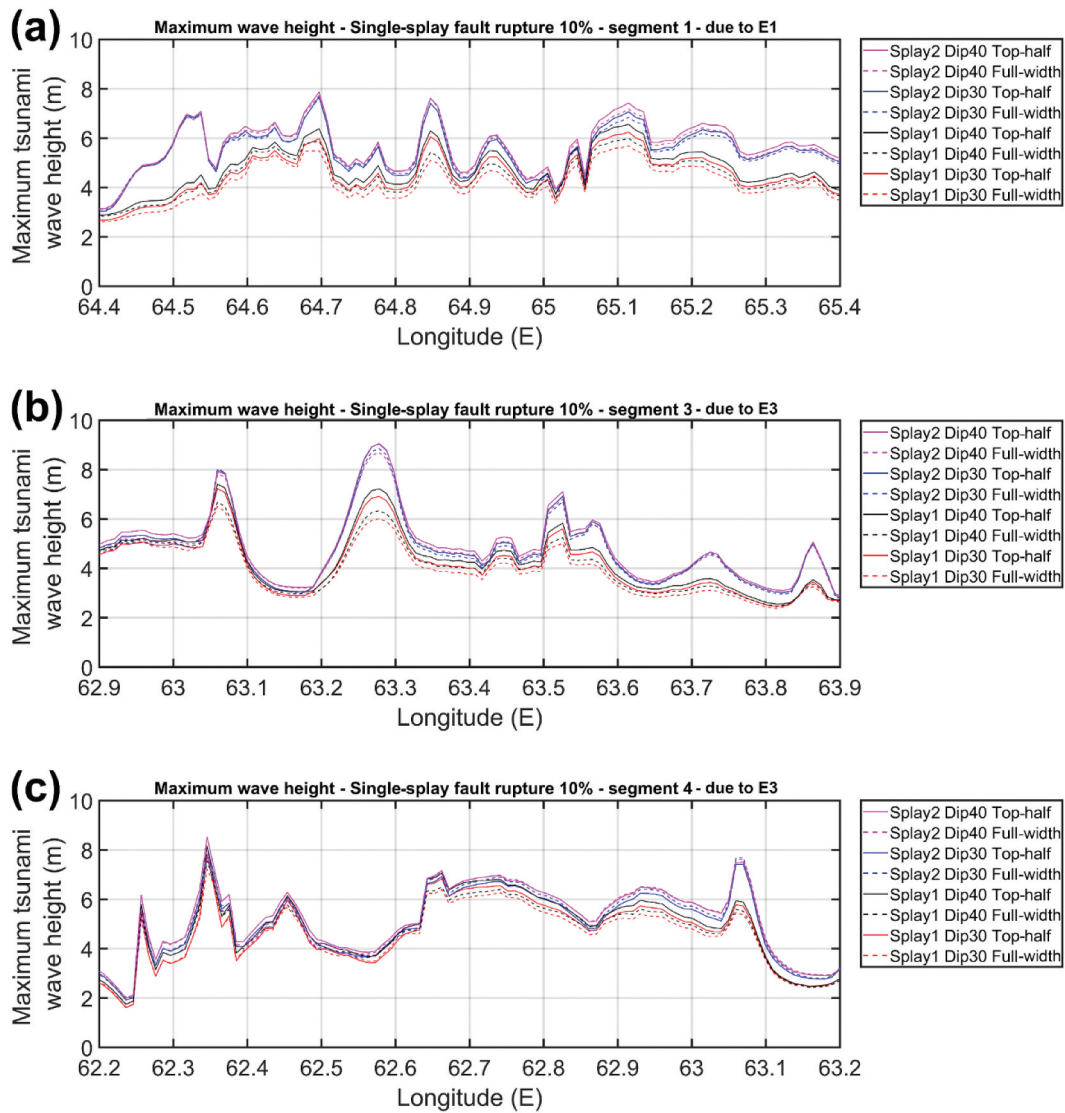


Figure 17. Maximum wave heights of the single-splay fault rupture scenario for the most affected coastal areas of: (a) segment 1, (b) segment 3, and (c) segment 4.

For brevity, due to the similarity between the results of single-splay and two-splay fault scenarios, only the single-splay fault results are presented. Figures 20 and 21 show the mean of the maximum wave heights and amplifications due to different seismic moment split ratios of the single-splay fault scenario. The solid black lines represent the results due to the 10% split ratio and dashed black lines represent 5% and 15%. Table 5 shows the mean of the wave height amplifications for the most affected areas of segments 1, 3, and 4 due to different seismic moment split ratios of single-splay fault rupture. The results show that a 5% increase in the seismic moment split ratio (10% to 15%) results in 37% increase in wave height amplifications. Also, a 5% reduction in the seismic moment split ratio (10% to 5%) results in a 30% decrease in wave height amplifications. In other words, the uncertainty related to the seismic moment split ratio significantly affects the results in a way that even a 5% increase in the ratio,

significantly increases the tsunami hazard in the affected areas.

3.2. Stochastic sources

In this section, the results due to the rupture of stochastic sources are investigated. The main objectives of this section are to examine whether the differences between the results due to the rupture of main and splay faults are statistically significant and to consider the effect of slip heterogeneity on the results. Two critical configurations of single-splay fault rupture that generate the maximum (Splay2, Dip 40, Top-half rupture) and minimum (Splay 1, Dip 30, Full-width rupture) in an average sense (section 3–1–3) are selected to be compared with the main fault rupture. To exclude the effect of different seismic moment split ratios, the results are only generated for the 10% split ratio. For each

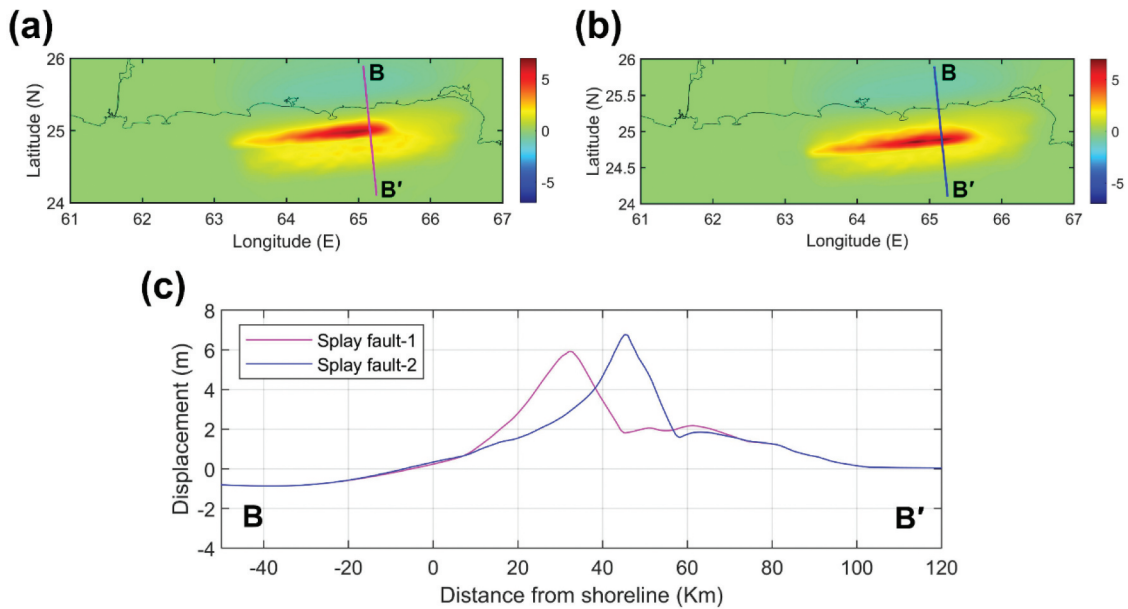


Figure 18. The vertical seabed deformation due to the rupture of: (a) E1 + splay fault-1 (b) E1 + splay fault-2. (c) Cross-section (B-B') of vertical seabed deformations due to the rupture of E1 + splay fault-1 and E1 + splay fault-2.

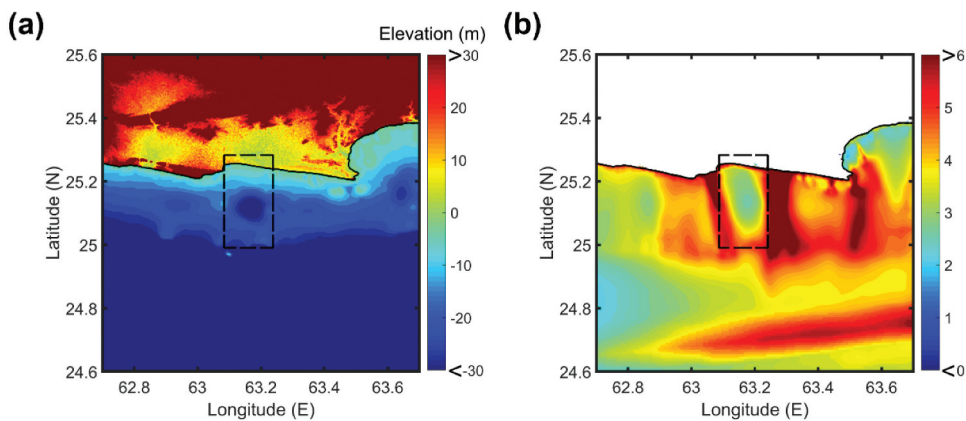


Figure 19. (a) Bathymetry and (b) maximum surface elevation heights (due to the single-splay fault rupture scenario of segment 3 and splay fault-2) for the areas around $63.1\text{E}-63.2\text{E}^\circ$ (dashed rectangles).

configuration, the tsunami simulations are performed for 1000 stochastic sources. To make the result section concise, only the results for segment 3 are presented.

3.2.1. Comparing results of stochastic sources of main and splay faults

Figure 22 shows the maximum wave heights due to the rupture of stochastic sources of main and combined main+splay faults over the entire shoreline (Figure 22a) and the most affected areas of segment 3 (Figure 22b). The results for the most affected areas indicate that at three percentile levels (5th, 50th, and 95th), the maximum wave heights due to combined main+splay rupture of D40 S2 Top-half is greater than D30 S1 Full-width and both of them are greater than the main fault rupture, which is consistent with the results of average sources (section 3-1-3).

To examine whether the differences between the results of the main and combined main+splay faults are statistically significant, the two-sample Kolmogorov–Smirnov test (KS-2 test) is performed over the most affected areas of segment 3 ($62.9\text{E}-63.9\text{E}^\circ$) (Berger and Zhou 2014; Massey 1951). These areas include 101 observational points and at each point, 1000 maximum wave heights due to rupture of the main fault and two sets of 1000 maximum wave heights due to rupture of two configurations of combined main+splay faults are generated (D40 S2 Top-half and D30 S1 Full-width). The KS-2 test determines a rejection of the null hypothesis that two samples of data are from the same distribution. In other words, if the result of the KS-2 test rejects the null hypothesis, it means that the difference between the two samples of data is statistically significant. The p values of the KS-2 test lie in the range of (0,1) and represent the probability of observing a test statistic as extreme as, or more

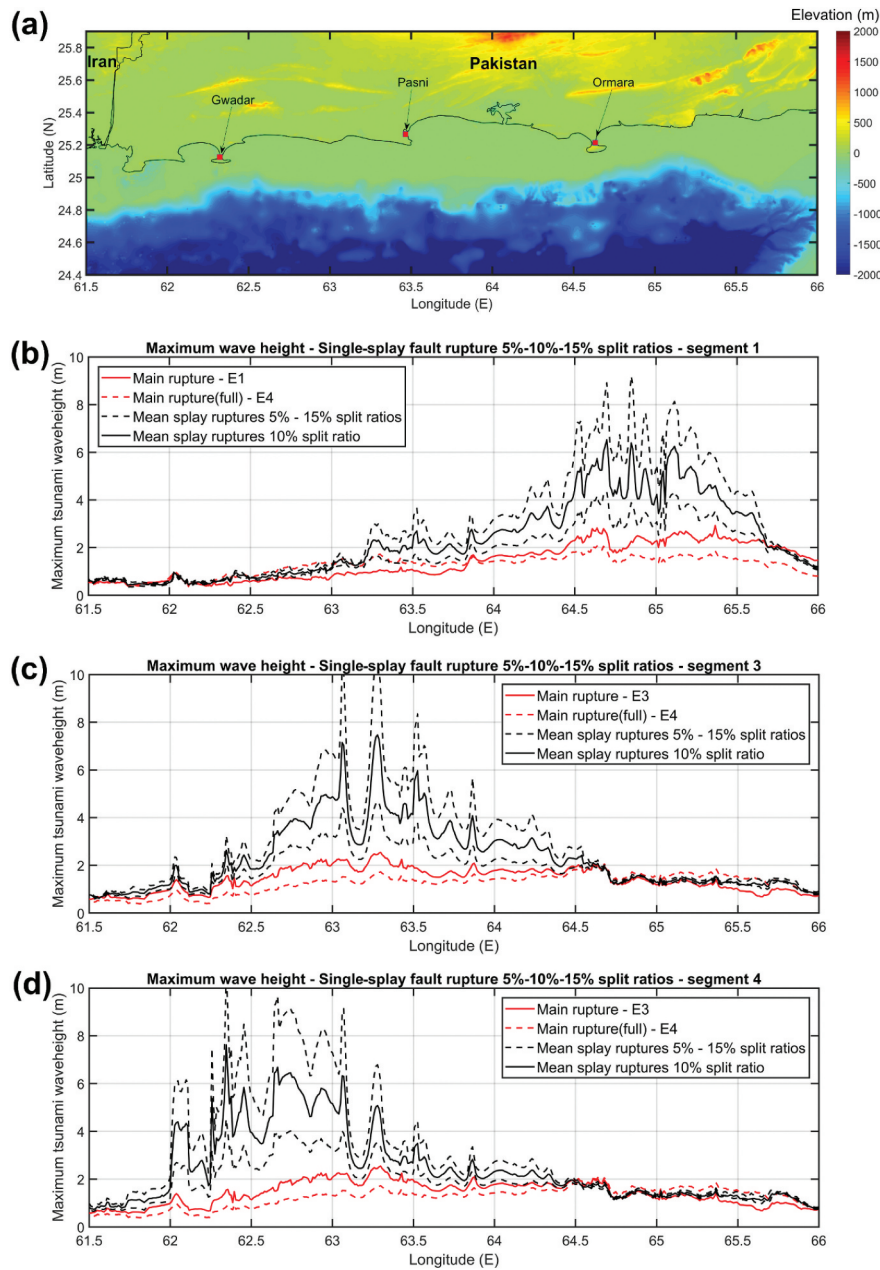


Figure 20. The maximum wave height results of single-splay fault rupture scenario due to different seismic moment split ratios (5%, 10%, and 15%).

extreme than, the observed value under the null hypothesis. Therefore, the smaller p values (close to 0) indicate a statistically significant difference between the two samples of data (Berger and Zhou 2014; Massey 1951). For each of the 101 points, the KS-2 test is performed for the two sets with different splay fault ruptures, and the respective p values are obtained. The results are shown in Figure 22c. Based on the small p values of both tests, the results due to the main fault and both combined main +splay faults are statistically different.

3.2.2. Effect of slip heterogeneity on tsunami hazard

The maximum wave height data for the specific point at 63.55E° is analyzed. Figure 23 shows the Box plot

(Figure 23a) and histograms (Figure 23b-d) of maximum wave heights at 63.55E°. The Box plot is a method of illustrating the locality, spread, and skewness of numerical data by their quartiles in descriptive statistics (DuToit, Steyn, and Stumpf 2012). The locality and spread of the maximum wave heights generated by main rupture and combined main+splay faults are visually different and all of them show a significant number of outliers (red points in Figure 23a) that represent extremely high values of the maximum wave height at 63.55E°. These extreme values are due to the effect of slip heterogeneity in the stochastic main and splay ruptures. In other words, the location of large-slip areas and amount of slip values, which are critical factors in determining the maximum wave height at a certain location, are significantly varied

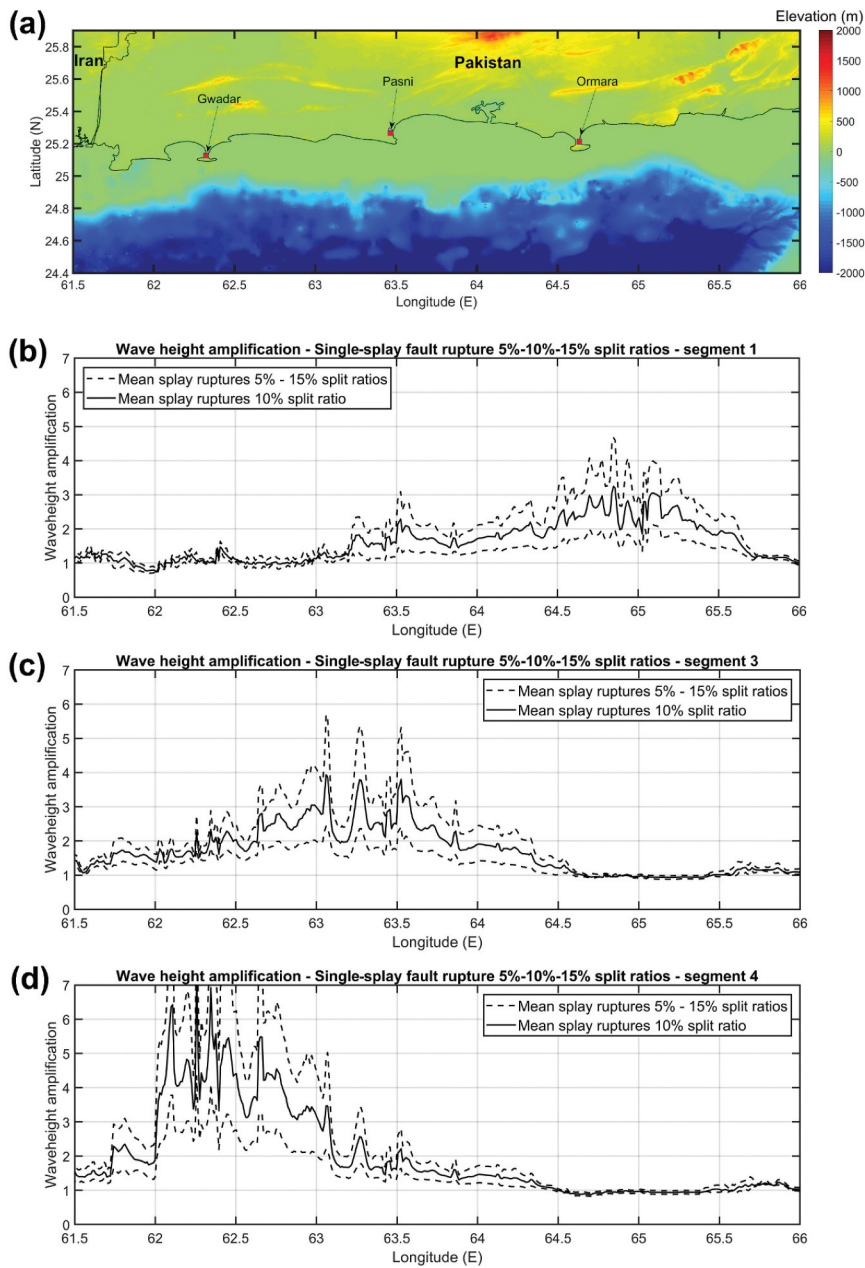


Figure 21. The wave height amplification results (parameter A in Equation 1) of single-splay fault rupture scenario due to different seismic moment split ratios (5%, 10%, and 15%).

among the stochastic sources. As a result, the stochastic sources that have large-slip areas in front of a certain point produce extremely high maximum wave heights. This topic is discussed in more detail in

Table 5. Mean of the wave height amplifications for the most affected areas of segments 1, 3, and 4 due to different seismic moment split ratios of single-splay fault rupture.

	Single-splay fault rupture		
	5% seismic momentsplit ratio	10% seismic momentsplit ratio	15% seismic momentsplit ratio
Segment 1	1.72	2.44	3.23
Segment 3	1.81	2.57	3.48
Segment 4	2.59	3.96	5.59

the following paragraphs. The histograms of maximum wave heights at 63.55° (Figure 23b-d) show a distribution with right tail skewness that indicates the presence of higher values with a relatively lower number of stochastic sources. Table 6 compares the mean and maximum predicted values of tsunami wave height by using average sources (section 3-1-3, Figure 17b) and stochastic sources (Figure 23a) at 63.55° . The predicted values by stochastic sources are significantly larger than average sources. This clearly shows the necessity of considering the effect of heterogeneous slip distributions through stochastic sources to predict the maximum wave height at a certain location. In other words, since the average sources do not account for the uncertainty of slip

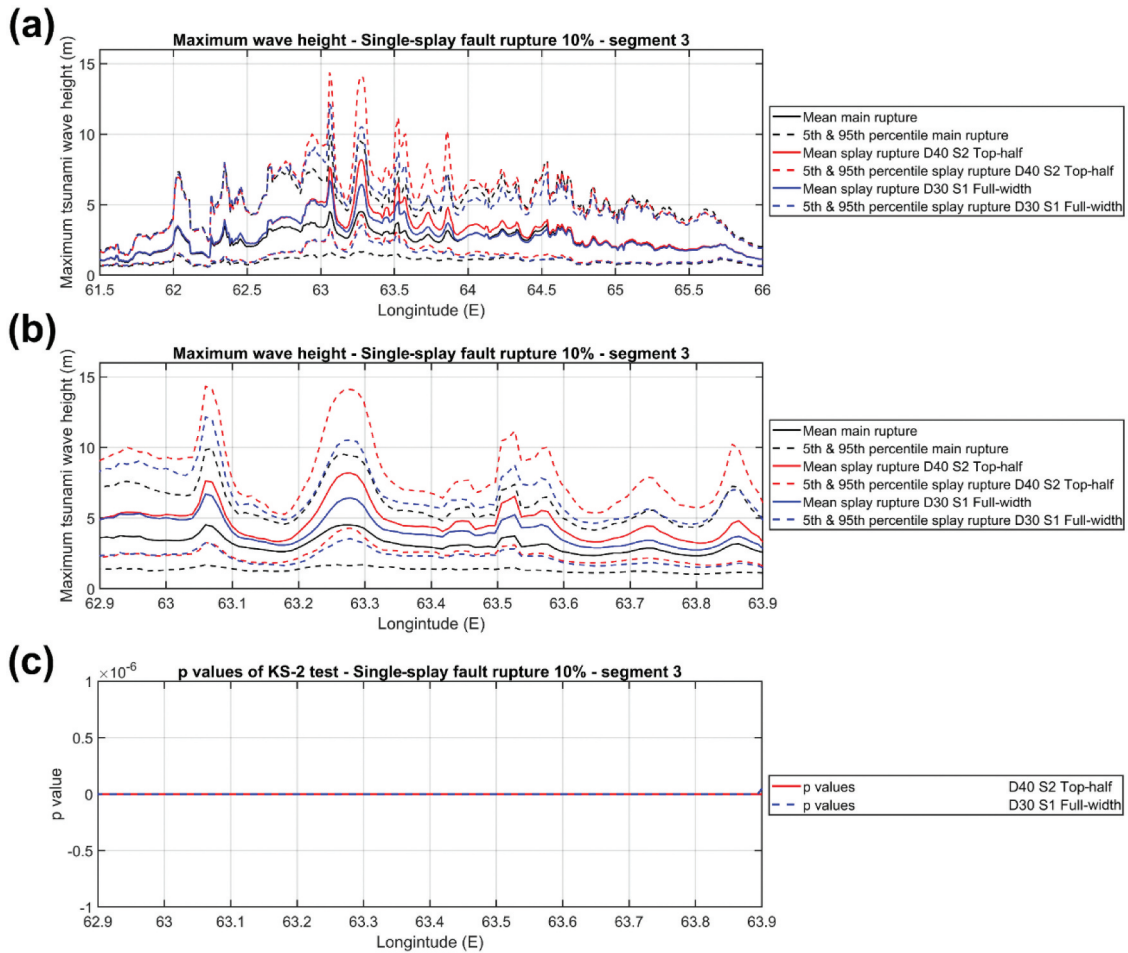


Figure 22. (a) Maximum wave heights of single-splay fault rupture scenario due to rupture of stochastic sources of segment 3. (b) Maximum wave heights of the single-splay fault rupture scenario due to rupture of stochastic sources for the most affected coastal areas segment 3. (c) P values of KS-2 test for the maximum wave heights due to rupture on the main plate boundary and single-splay fault rupture scenario of segment 3.

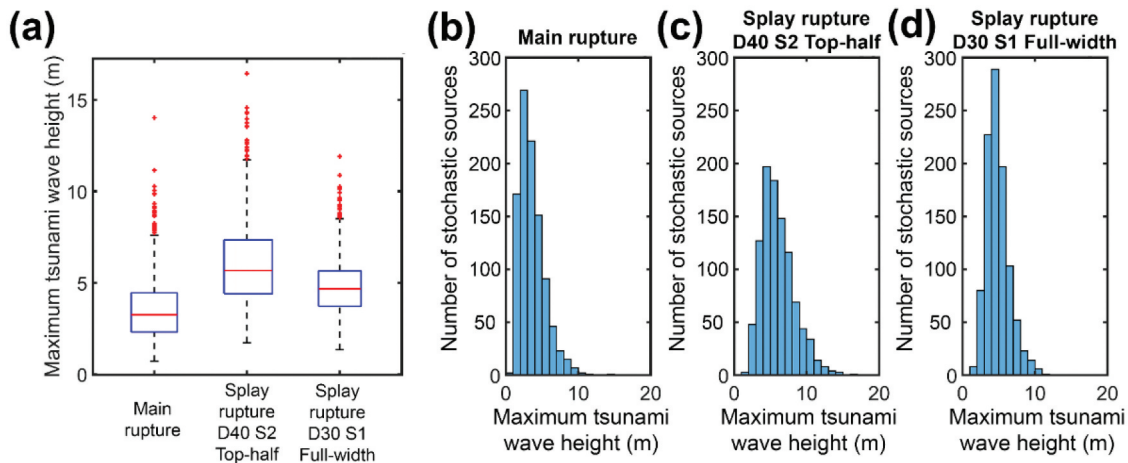


Figure 23. (a) Box plot of the maximum wave heights at 63.55° due to the single-splay fault rupture of stochastic sources of segment 3. Normalized PDF of maximum wave heights at 63.55° due to the single-splay fault rupture of stochastic sources of segment 3: (b) Main plate boundary, (c) Combined main+Splay2 Dip 40 Top-half, and (d) Combined main+Splay1 Dip 30 Full-width.

Table 6. Mean and maximum predicted values of tsunami wave height by average sources and stochastic sources at 63.55E°.

	Average sources	Stochastic sources
Mean predicted value	4.0 m	4.8 m
Maximum predicted value	5.5 m	17 m

distribution heterogeneity, their predicted wave heights are not the maximum, and further investigations using stochastic sources are necessary.

Figure 24 shows the scatter plot of the maximum wave height at 63.55E° due to rupture of stochastic sources of the main and corresponding combined main+splay faults (D40 S2 Top-half and D30 S1 Full-width). The results above the dashed yellow lines indicate that the combined main+splay faults stochastic sources produce greater maximum wave heights compared to their corresponding main fault stochastic sources (wave height amplification > 1). The red circles that represent the results related to D40 S2 Top-half indicate greater maximum wave heights compared to the results related to D30 S1 Full-width, which is consistent with the conclusions that have been drawn in section 3–1-3 using average sources.

Figure 25a shows the scatter plot of wave height amplifications due to the stochastic sources rupture of combined main+splay faults (D40 S2 Top-half and D30 S1 Full-width) and maximum wave heights due to their corresponding main

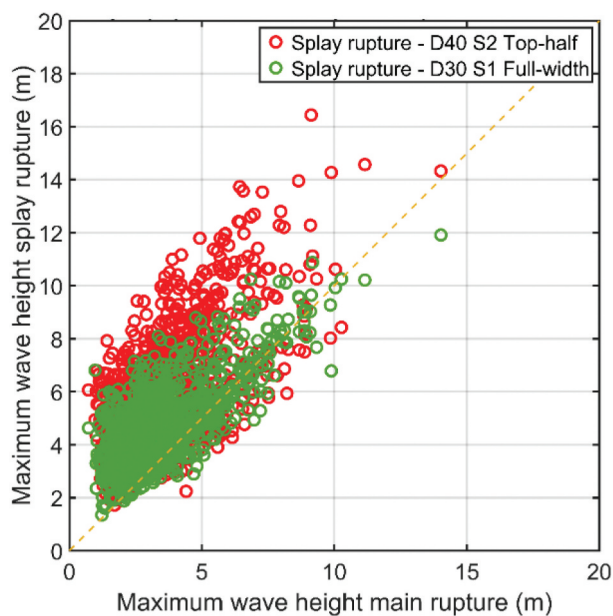


Figure 24. Scatter plot of the maximum wave height at 63.55E° due to stochastic sources rupture of the main plate boundary and the corresponding single-splay fault ruptures of segment 3.

fault stochastic sources at 63.55E°. The results above the dashed green line represent the combined main+splay stochastic sources that generate wave height amplification greater than 1. The probability of amplification >1 due to each combined main+splay faults configuration equals the ratio of the number of stochastic sources (red or green circles) that generate amplifications > 1 to the total number of stochastic sources (1000). The aforementioned probability for the D40 S2 Top-half configuration is greater than the D30 S1 Full-width configuration (0.922 vs 0.802) which is consistent with the results of the average sources (section 3–1-3).

The stars and diamonds in Figure 25a indicate the 5th, 50th, and 95th percentiles of wave height amplifications due to both configurations of the combined main+splay faults. Figure 25b-d show the combined main+splay stochastic sources (D40 S2 Top-half) that are responsible for the 5th, 50th, and 95th percentiles of wave height amplifications. The significant difference between the 5th, and 95th percentiles values (0.93 vs. 3.46) is due to the slip heterogeneity of the main fault plane and more specifically, the location of the large-slip areas on the fault plane. Generally, the combined main+splay stochastic sources that generate greater amplifications (vertical axis of Figure 25a) relate to the lower wave heights (horizontal axis of Figure 25a) due to their corresponding main fault stochastic source and vice versa. In other words, the main fault stochastic sources that have large-slip areas in front of a specific point (in this case 63.55E°) are associated with lower amplifications which means that the splay fault rupture does not always result in greater hazards (Figure 25d). On the other hand, the stochastic sources that do not have large-slip areas in front of 63.55E° lead to higher amplifications, which means that the splay fault ruptures increase the hazard significantly (Figure 25b).

4. Conclusions

In this study, the effects of the rupture of splay faults on the tsunami hazard of eastern MSZ were studied by developing the novel and comprehensive framework that uses the logic tree and stochastic earthquake rupture models and considers uncertainties related to rupture location, rupture geometry, seismic moment split ratio, earthquake slip asperity location within a fault plane, and earthquake slip heterogeneity. The results of this study were generated in two parts by using average source models and stochastic source models. In the average source models part, the effects of

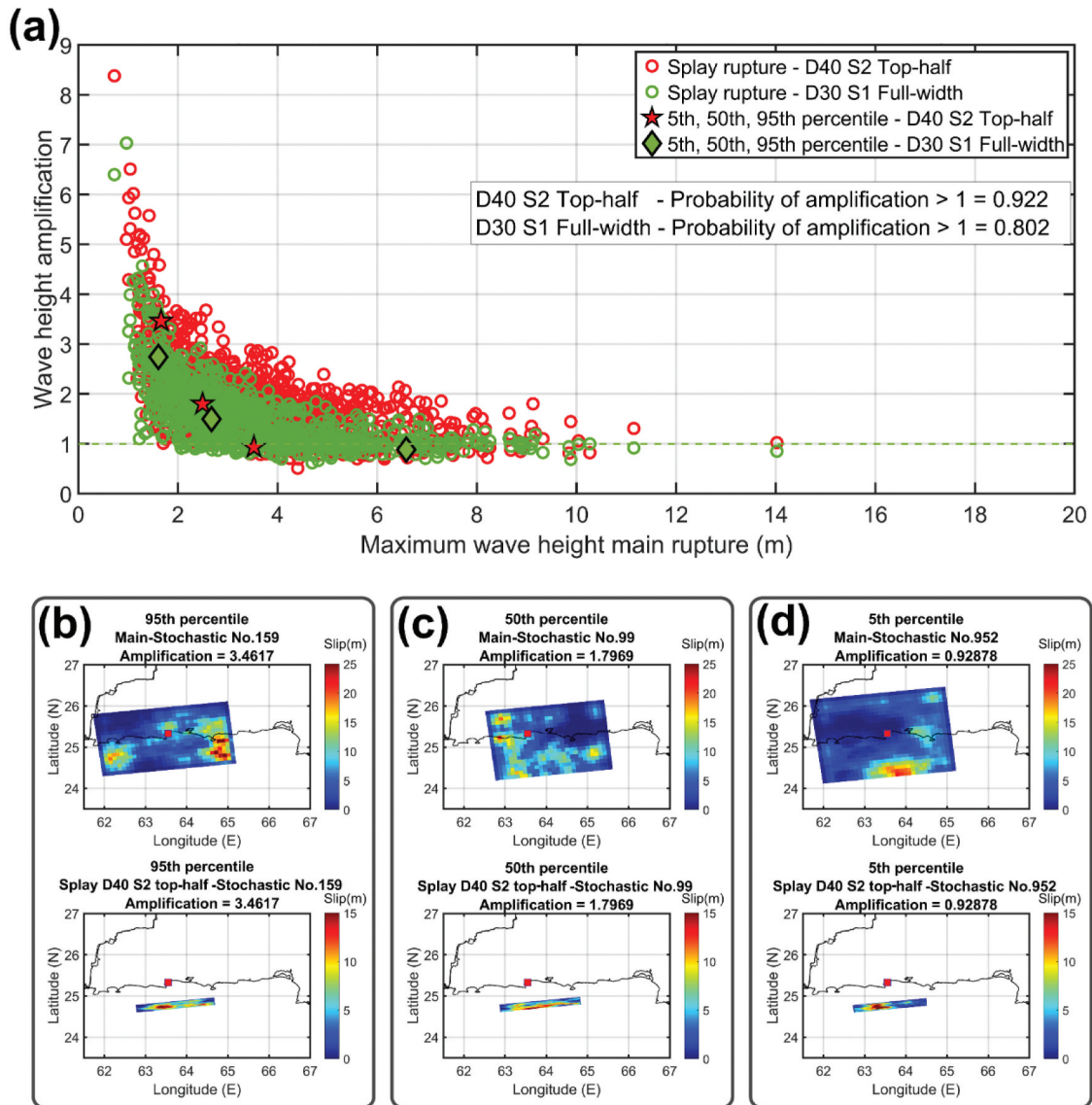


Figure 25. (a) Scatter plot of wave height amplifications due to the stochastic sources rupture of single-splay fault scenario of segment 3 and maximum wave heights due to main plate boundary rupture at 63.55° . Main plate boundary and splay fault stochastic sources that are responsible for the: (b) 95th percentile of wave height amplification, (c) 50th percentile of wave height amplification, and (d) 5th percentile of wave height amplification.

rupture of splay faults as well as their different characteristics (dip, location, asperity, and seismic moment split ratio) were investigated and the most critical parameters within those varied were identified. In the second part, several critical configurations of the main fault rupture and splay fault rupture were selected, and a complete set of tsunami simulations using the stochastic sources was conducted by considering the effect of earthquake slip heterogeneity. It was assumed that the rupture on the plate boundary fault plane triggers the ruptures on the splay faults and they occur concurrently. The moment magnitude of 8.6 was considered as a scenario magnitude and the geometry of splay faults was obtained using the most recent studies of the tectonic structures of the MSZ including offshore multi-channel seismic reflection data.

Our results due to the rupture of average sources showed a significant impact of splay faults on the maximum tsunami heights; for instance, we observed 4.5 m difference in tsunami heights, and an amplification factor of 4 for areas around Pasni for the single-splay fault rupture. Generally, the effects of rupture of the single-splay fault scenario were greater than the two-splay fault scenario. Also, the location of the splay faults was identified as the most critical factor among the splay fault characteristics. Other impactful factors were the dip angles, asperities, and fault width. As an example, in the same scenario and same seismic moment split ratio, the splay faults that are located over the high slip areas of the main fault, experience top-half asperities and have steeper dip angles are the worst scenarios that generate the largest tsunami heights. Furthermore, uncertainty in the seismic moment split ratio significantly affects the tsunami hazard in a way that 5% increase in the seismic

moment split ratio (10% to 15%) results in 37% increase in wave height amplifications at a specified point (63.55E°). The results due to rupture of stochastic sources showed that the differences between the results of the main and combined (i.e. main and splay) faults are statistically significant. Also, due to the effect of earthquake slip heterogeneity, the predicted values by stochastic sources are significantly larger than average sources. These results clearly show the necessity of considering the effect of heterogeneous slip distributions through stochastic sources to accurately predict the maximum wave height. It should be noted that for similar studies focusing on other regions, the locations of splay faults and their dip angles should be evaluated carefully. Our results showed that splay faults can amplify tsunami heights in the Makran region by 3–9 times as compared to ruptures exclusively on the plate boundary.

As for future studies, instead of considering several critical configurations for stochastic sources, more extensive sensitivity analyses can be conducted to analyze the effect of rupture of stochastic sources and to evaluate the maximum predicted values for the entire shoreline by considering the heterogeneous slip distributions. The effect of the seismic moment split ratio can be investigated further, as it does have a significant impact on the tsunami hazard. Moreover, the uncertainties related to the moment magnitude of the main fault and different scaling relationships can be incorporated into the logic tree as epistemic uncertainties. The aforementioned uncertainties can also be studied by utilizing a comprehensive analysis of the geological and geophysical characteristics of the Makran region. Finally, coastal damage assessment due to the inundation of important ports using more accurate local bathymetry datasets of nearshore shallow water areas is an important topic for future research. We recommend that the study area to be extended to cover west Makran and eventually the entire Makran region in future studies.

Acknowledgments

KG is funded by the Canada Research Chairs program (950-232015) and the NSERC Discovery Grant (RGPIN-2019-05898). MH is funded by the Royal Society, the United Kingdom, grant number CHL/R1/180173.

Disclosure statement

No potential conflict of interest was reported by the author(s).

Funding

This work was supported by the NSERC Discovery Grant [RGPIN-2019-05898]; Canada Research Chairs program [950-232015]; Royal Society [CHL/R1/180173].

ORCID

Payam Momeni  <http://orcid.org/0000-0001-8704-8346>
Katsuchihiro Goda  <http://orcid.org/0000-0003-3900-2153>

References

- Allen, T. I., and G. P. Hayes. 2017. "Alternative Rupture-scaling Relationships for Subduction Interface and Other Offshore Environments." *Bulletin of the Seismological Society of America* 107 (3): 1240–1253. doi:10.1785/0120160255.
- Annaka, T., K. Satake, T. Sakakiyama, K. Yanagisawa, and N. Shuto. 2007. "Logic-tree Approach for Probabilistic Tsunami Hazard Analysis and Its Applications to the Japanese Coasts." *Tsunami and Its Hazards in the Indian and Pacific Oceans* 577–592. doi:10.1007/978-3-7643-8364-0_17.
- Baba, T., Ph. Cummins, and R. Hori, , and Y. Kaneda (2006). High Precision Slip Distribution of the 1944 Tonankai Earthquake Inferred from Tsunami Waveforms: Possible Slip on a Splay Fault, *Tectonophysics*, 426, 119–134, doi:10.1016/j.tecto.2006.02.015.
- Berger, V. W., and Y. Zhou. 2014. "Kolmogorov–Smirnov Test: Overview." *Wiley Statsref: Statistics Reference Online*. doi:10.1002/9781118445112.stat06558.
- Box, G. EP., and D. R. Cox. 1964. "An Analysis of Transformations." *Journal of the Royal Statistical Society: Series B (Methodological)* 26 (2): 211–243. doi:10.1111/j.2517-6161.1964.tb00553.x.
- Byrne, D. E., L. R. Sykes, and D. M. Davis. 1992. "Great Thrust Earthquakes and Aseismic Slip along the Plate Boundary of the Makran Subduction Zone." *Journal of Geophysical Research: Solid Earth* 97 (B1): 449–478. doi:10.1029/91JB02165.
- Clarke, S. H., and G. A. Carver. 1992. "Late Holocene Tectonics and Paleoseismicity, Southern Cascadia Subduction Zone." *Science* 255 (5041): 188–192. doi:10.1126/science.255.5041.188.
- Coppersmith, K. J., and R. R. Youngs. 1986. "Capturing Uncertainty in Probabilistic Seismic Hazard Assessments within Intraplate Tectonic Environments." *Proceedings of the Third US national conference on earthquake engineering*, Charleston, SC, USA. 1: 301–312.
- Courant, R., K. Friedrichs, and H. Lewy. 1967. "On the Partial Difference Equations of Mathematical Physics." *IBM Journal of Research and Development* 11 (2): 215–234. doi:10.1147/rd.112.0215.
- Cummins, P. R., and Y. Kaneda. 2000. "Possible Splay Fault Slip during the 1946 Nankai Earthquake." *Geophysical Research Letters* 27 (17): 2725–2728. doi:10.1029/1999GL011139.
- DuToit, S. H., A. G. W. Steyn, and R. H. Stumpf. 2012. *Graphical Exploratory Data Analysis*. Berlin/Heidelberg, Germany: Springer Science & Business Media.
- El-Hussain, I., R. Omira, Z. Al-Habsi, M. A. Baptista, A. Deif, and A. M. E. Mohamed. 2018. "Probabilistic and Deterministic Estimates of Near-Field Tsunami Hazards in Northeast Oman." *Geoscience Letters* 5 (1): 1–13. doi:10.1186/s40562-018-0129-4.
- El-Hussain, I., R. Omira, A. Deif, Z. Al-Habsi, G. Al-Rawas, A. Mohamad, K. Al-Jabri, and M. A. Baptista. 2016. "Probabilistic Tsunami Hazard Assessment along Oman Coast from Submarine Earthquakes in the Makran Subduction Zone." *Arabian Journal of Geosciences* 9 (15): 1–14. doi:10.1007/s12517-016-2687-0.

- Fukao, Y. 1979. "Tsunami Earthquakes and Subduction Processes near Deep-sea Trenches." *Journal of Geophysical Research: Solid Earth* 84 (B5): 2303–2314. doi:10.1029/JB084iB05p02303.
- Fukutani, Y., A. Suppasri, and F. Imamura. 2015. "Stochastic Analysis and Uncertainty Assessment of Tsunami Wave Height Using a Random Source Parameter Model that Targets a Tohoku-Type Earthquake Fault." *Stochastic Environmental Research and Risk Assessment* 29 (7): 1763–1779. doi:10.1007/s00477-014-0966-4.
- GEBCO. 2021. *The GEBCO_2021 Grid: A Continuous Terrain Model of the Global Oceans and Land*. NERC EDS British Oceanographic Data Centre NOC. doi:10.5285/c6612cbe-50b3-0cff-e053-6c86abc09f8f.
- Goda, K., T. Yasuda, N. Mori, and T. Maruyama. 2016. "New Scaling Relationships of Earthquake Source Parameters for Stochastic Tsunami Simulation." *Coastal Engineering Journal* 58 (3): 1650010–1650011. doi:10.1142/S0578563416500108.
- González, J., G. González, R. Aránguiz, D. Melgar, N. Zamora, M. N. Shrivastava, R. Das, P. A. Catalán, and R. Cienfuegos. 2020. "A Hybrid Deterministic and Stochastic Approach for Tsunami Hazard Assessment in Iquique, Chile." *Natural Hazards* 100 (1): 231–254. doi:10.1007/s11069-019-03809-8.
- Goto, C., Y. Ogawa, N. Shuto, and F. Imamura. 1997. "Numerical Method of Tsunami Simulation with the Leap-Frog Scheme." *IUGG/IOC TIME Project Intergovernmental Oceanographic Commission of UNESCO, Manuals and Guides* 35: 130.
- Grando, G., and K. McClay. 2007. "Morphotectonics Domains and Structural Styles in the Makran Accretionary Prism, Offshore Iran." *Sedimentary Geology* 196 (1–4): 157–179. doi:10.1016/j.sedgeo.2006.05.030.
- Hayes, G. P., G. L. Moore, D. E. Portner, M. Hearne, H. Flamme, M. Furtney, and G. M. Smoczyk. 2018. "Slab2, a Comprehensive Subduction Zone Geometry Model." *Science* 362 (6410): 58–61. doi:10.1126/science.aat4723.
- Heidarzadeh, M., T. Ishibe, T. Harada, D. H. Natawidjaja, I. R. Pranantyo, and B. T. Widyantoro. 2021. "High Potential for Splay Faulting in the Molucca Sea, Indonesia: November 2019 Mw 7.2 Earthquake and Tsunami." *Seismological Research Letters* 92 (5): 2915–2926. doi:10.1785/0220200442.
- Heidarzadeh, M., M. D. Pirooz, and N. H. Zaker. 2009. "Modeling the Near-Field Effects of the Worst-Case Tsunami in the Makran Subduction Zone." *Ocean Engineering* 36 (5): 368–376. doi:10.1016/j.oceaneng.2009.01.004.
- Heidarzadeh, M., M. D. Pirooz, N. H. Zaker, A. C. Yalciner, M. Mokhtari, and A. Esmaeily. 2008. "Historical Tsunami in the Makran Subduction Zone off the Southern Coasts of Iran and Pakistan and Results of Numerical Modeling." *Ocean Engineering* 35 (8–9): 774–786. doi:10.1016/j.oceaneng.2008.01.017.
- Heidarzadeh, M., and K. Satake. 2014. "Possible Sources of the Tsunami Observed in the Northwestern Indian Ocean following the 2013 September 24 Mw 7.7 Pakistan Inland Earthquake." *Geophysical Journal International* 199 (2): 752–766. doi:10.1093/gji/ggu297.
- Heidarzadeh, M., and K. Satake. 2017. "A Combined Earthquake–Landslide Source Model for the Tsunami from the 27 November 1945 M W 8.1 Makran Earthquake." *Bulletin of the Seismological Society of America* 107 (2): 1033–1040. doi:10.1785/0120160196.
- Hoechner, A., A. Y. Babeyko, and N. Zamora. 2016. "Probabilistic Tsunami Hazard Assessment for the Makran Region with Focus on Maximum Magnitude Assumption." *Natural Hazards and Earth System Sciences (NHES)* 16: 1339–1350. doi:10.5194/nhess-16-1339-2016.
- Horspool, N., I. Pranantyo, J. Griffin, H. Latief, D. H. Natawidjaja, W. Kongko, A. Cipta, B. Bustaman, S. D. Anugrah, and H. K. Thio. 2014. "A Probabilistic Tsunami Hazard Assessment for Indonesia." *Natural Hazards and Earth System Sciences (NHES)* 14 (11): 3105–3122. doi:10.5194/nhess-14-3105-2014.
- Hsu, Y., M. Simons, J. P. Avouac, J. Galetzka, K. Sieh, M. Chlieh, D. Natawidjaja, L. Prawirodirdjo, and Y. Bock. 2006. "Frictional Afterslip following the 2005 Nias-Simeulue Earthquake, Sumatra." *Science* 312 (5782): 1921–1926. doi:10.1126/science.1126960.
- Jaiswal, R. K., A. P. Singh, and B. K. Rastogi. 2009. "Simulation of the Arabian Sea Tsunami Propagation Generated Due to 1945 Makran Earthquake and Its Effect on Western Parts of Gujarat (India)." *Natural Hazards* 48 (2): 245–258. doi:10.1007/s11069-008-9261-3.
- Kame, N., and T. Yamashita. 1999. "Simulation of the Spontaneous Growth of a Dynamic Crack without Constraints on the Crack Tip Path." *Geophysical Journal International* 139 (2): 345–358. doi:10.1046/j.1365-246x.1999.00940.x.
- Lorito, S., J. Selva, R. Basili, F. Romano, M. M. Tiberti, and A. Piatanesi. 2015. "Probabilistic Hazard for Seismically Induced Tsunamis: Accuracy and Feasibility of Inundation Maps." *Geophysical Journal International: 2001* 200 (1): 574–588. doi:10.1093/gji/ggu408.
- Mai, P. M., and G. C. Beroza. 2002. "A Spatial Random Field Model to Characterize Complexity in Earthquake Slip." *Journal of Geophysical Research: Solid Earth* 107 (B11): ESE–10. doi:10.1029/2001JB000588.
- Mai, P. M., and K. K. S. Thingbaijam. 2014. "SRCMOD: An Online Database of Finite-fault Rupture Models." *Seismological Research Letters* 85 (6): 1348–1357. doi:10.1785/0220140077.
- Massey, F. J., Jr. 1951. "The Kolmogorov-Smirnov Test for Goodness of Fit." *Journal of the American Statistical Association* 46 (253): 68–78. doi:10.1080/01621459.1951.10500769.
- Mokhtari, M. 2015. "The Role of Splay Faulting in Increasing the Devastation Effect of Tsunami Hazard in Makran, Oman Sea." *Arabian Journal of Geosciences* 8 (7): 4291–4298. doi:10.1007/s12517-014-1375-1.
- Mokhtari, M., I. A. Fard, and K. Hessami. 2008. "Structural Elements of the Makran Region, Oman Sea and Their Potential Relevance to Tsunamiogenesis." *Natural Hazards* 47 (2): 185–199. doi:10.1007/s11069-007-9208-0.
- Momeni, P., K. Goda, M. Heidarzadeh, and J. Qin. 2020. "Stochastic Analysis of Tsunami Hazard of the 1945 Makran Subduction Zone Mw 8.1–8.3 Earthquakes." *Geosciences* 10 (11): 452. doi:10.3390/geosciences10110452.
- Mori, N., A. Muhammad, K. Goda, T. Yasuda, and A. Ruiz-Angulo. 2017. "Probabilistic Tsunami Hazard Analysis of the Pacific Coast of Mexico: Case Study Based on the 1995 Colima Earthquake Tsunami." *Frontiers in Built Environment* 3: 34. doi:10.3389/fbuil.2017.00034.
- Murotani, S., K. Satake, and Y. Fujii. 2013. "Scaling Relations of Seismic Moment, Rupture Area, Average Slip, and Asperity Size for M~ 9 Subduction-zone Earthquakes." *Geophysical Research Letters* 40 (19): 5070–5074. doi:10.1002/grl.50976.
- Neetu, S., I. Suresh, R. Shankar, B. Nagarajan, R. Sharma, S. S. C. Sheno, A. S. Unnikrishnan, and D. Sundar. 2011. "Trapped Waves of the 27 November 1945 Makran Tsunami: Observations and Numerical Modeling." *Natural Hazards* 59 (3): 1609–1618. doi:10.1007/s11069-011-9854-0.

- Okada, Y. 1985. "Surface Deformation Due to Shear and Tensile Faults in a Half-Space." *Bulletin of the Seismological Society of America* 75 (4): 1135–1154. doi:10.1785/BSSA0750041135.
- Okal, E. A., and C. E. Synolakis. 2008. "Far-field Tsunami Hazard from mega-thrust Earthquakes in the Indian Ocean." *Geophysical Journal International* 172 (3): 995–1015. doi:10.1111/j.1365-246X.2007.03674.x.
- Pajang, S., N. Cubas, J. Letouzey, L. L. Pourhiet, S. Seyedali, M. Fournier, P. Agard, M. M. Khatib, M. Heyhat, and M. Mokhtari. 2021. "Seismic Hazard of the Western Makran Subduction Zone: Insight from Mechanical Modelling and Inferred Frictional Properties." *Earth and Planetary Science Letters* 562: 116789. doi:10.1016/j.epsl.2021.116789.
- Park, J., T. Tsuru, S. Kodaira, P. R. Cummins, and Y. Kaneda. 2002. "Splay Fault Branching along the Nankai Subduction Zone." *Science* 297 (5584): 1157–1160. doi:10.1126/science.1074111.
- Penney, C., F. Tavakoli, A. Saadat, H. R. Nankali, M. Sedighi, F. Khorrami, F. Sobouti, Z. Rafi, A. Copley, and J. Jackson. 2017. "Megathrust and Accretionary Wedge Properties and Behaviour in the Makran Subduction Zone." *Geophysical Journal International* 209 (3): 1800–1830. doi:10.1093/gji/ggx126.
- Plafker, G. 1972. "Alaskan Earthquake of 1964 and Chilean Earthquake of 1960: Implications for Arc Tectonics." *Journal of Geophysical Research* 77 (5): 901–925. doi:10.1029/JB077i005p00901.
- Rashidi, A., D. Dutykh, N. Keshavarz, and L. Audin. 2021. "Regional Tsunami Hazard from Splay Faults in the Gulf of Oman." *Ocean Engineering* 243: 110169. doi:10.1016/j.oceaneng.2021.110169.
- Rashidi, A., Z. H. Shomali, D. Dutykh, and N. K. Farajkhah. 2020. "Tsunami Hazard Assessment in the Makran Subduction Zone." *Natural Hazards* 100 (2): 861–875. doi:10.1007/s11069-019-03848-1.
- Satake, K. 1995. "Linear and Nonlinear Computations of the 1992 Nicaragua Earthquake Tsunami." *Pure and Applied Geophysics* 144 (3): 455–470. doi:10.1007/BF00874378.
- Sibuet, J., C. Rangin, X. L. Pichon, S. Singh, A. Cattaneo, D. Graindorge, F. Klingelhoefer, J. Lin, J. Malod, and T. Maury. 2007. "26th December 2004 Great Sumatra–Andaman Earthquake: Co-Seismic and Post-Seismic Motions in Northern Sumatra." *Earth and Planetary Science Letters* 263 (1–2): 88–103. doi:10.1016/j.epsl.2007.09.005.
- Smith, G. L. 2013. "The Structure, Fluid Distribution and Earthquake Potential of the Makran Subduction Zone, Pakistan." PhD Thesis. University of Southampton.
- Smith, G. L., L. McNeill, T. J. Henstock, and J. Bull. 2012. "The Structure and Fault Activity of the Makran Accretionary Prism." *Journal of Geophysical Research: Solid Earth* 117: B7. doi:10.1029/2012JB009312.
- Sykes, L. R., and W. Menke. 2006. "Repeat Times of Large Earthquakes: Implications for Earthquake Mechanics and Long-Term Prediction." *Bulletin of the Seismological Society of America* 96 (5): 1569–1596. doi:10.1785/0120050083.
- Tanioka, Y., and K. Satake. 1996. "Tsunami Generation by Horizontal Displacement of Ocean Bottom." *Geophysical Research Letters* 23 (8): 861–864. doi:10.1029/96GL00736.
- USGS. 2015. "Shuttle Radar Topography Mission (SRTM) 1 Arc-Second Global." *US Geological Survey*.
- Wang, K., and Y. Hu. 2006. "Accretionary Prisms in Subduction Earthquake Cycles: The Theory of Dynamic Coulomb Wedge." *Journal of Geophysical Research: Solid Earth* 111 (B6). doi:10.1029/2005JB003987.
- Wells, D. L., and K. J. Coppersmith. 1994. "New Empirical Relationships among Magnitude, Rupture Length, Rupture Width, Rupture Area, and Surface Displacement." *Bulletin of the Seismological Society of America* 84 (4): 974–1002. doi:10.1785/BSSA0840040974.
- Woessner, J., and R. J. Farahani. 2020. "Tsunami Inundation Hazard across Japan." *International Journal of Disaster Risk Reduction* 49: 101654. doi:10.1016/j.ijdrr.2020.101654.